

# Synthesis and mechanical characterization of mechanically strong, polyurea-crosslinked, ordered mesoporous silica aerogels

Gitogo Churu<sup>1</sup> · Barbara Zupančič<sup>2</sup> · Dhairyashil Mohite<sup>3</sup> · Clarissa Wisner<sup>3</sup> · Huiyang Luo<sup>1</sup> · Igor Emri<sup>2</sup> · Chariklia Sotiriou-Leventis<sup>3</sup> · Nicholas Leventis<sup>3</sup> · Hongbing Lu<sup>1</sup>

Received: 22 October 2014 / Accepted: 11 March 2015 / Published online: 28 March 2015  
© Springer Science+Business Media New York 2015

**Abstract** Mechanically strong polymer-crosslinked templated silica aerogel (CTSA) monoliths with ordered tubular mesopores were synthesized through an acid-catalyzed, surfactant-templated sol–gel process followed by covalent crosslinking of the elementary building blocks with polyurea. Specifically, a structure-directing reagent (triblock copolymer, Pluronic P123) was used in combination with variable amounts of a micelle-swelling reagent (1,3,5-trimethylbenzene) to regulate the size, shape, morphology of the elementary building blocks, as well as the pore size distribution of acid-catalyzed silica. The structure was subsequently treated with variable

concentrations of a diisocyanate that reacts with surface –OH groups as well as residual gelation water adsorbed on the surface of silica. The developing polymer (polyurea) adheres to the walls of the mesoporous tubes and leaves macropores open. Rather than using a typical supercritical fluid (typically from CO<sub>2</sub>) drying protocol, the polymer-crosslinked materials of this study are strong enough to withstand stresses imposed by evaporating solvents and were dried from pentane under ambient pressure. The morphostructural properties of CTSAs were characterized before and after compression testing using a battery of methods including SEM, TEM and small-angle X-ray scattering. Mechanical properties were investigated using quasi-static compression tests, tensile, high-strain-rate dynamic tests as well as shear creep measurements. In addition, dynamic mechanical analysis as well as heat transfer tests was conducted. The Young's modulus was found to be about 800 MPa while the specific energy absorption was as high as 123 J/g, making this material a prime candidate for ballistic protection.

*Graphical abstract* Mechanically strong polymer-crosslinked templated silica aerogel (CTSA) monoliths with ordered tubular mesopores were synthesized through an acid-catalyzed, surfactant-templated sol–gel process followed by covalent crosslinking of the elementary building blocks with polyurea, leaving macropores open. Using pentane under ambient pressure drying protocol, the CTSAs are strong enough to withstand stresses imposed by evaporating solvents. The mechanical and morphostructural properties of CTSAs were characterized using SEM, TEM and small-angle X-ray scattering (SAXS). The Young's modulus was found to be about 800 MPa while the specific energy absorption was as high as 123 J/g, making this material a prime candidate for energy absorption under impact.

---

✉ Chariklia Sotiriou-Leventis  
cslevent@mst.edu

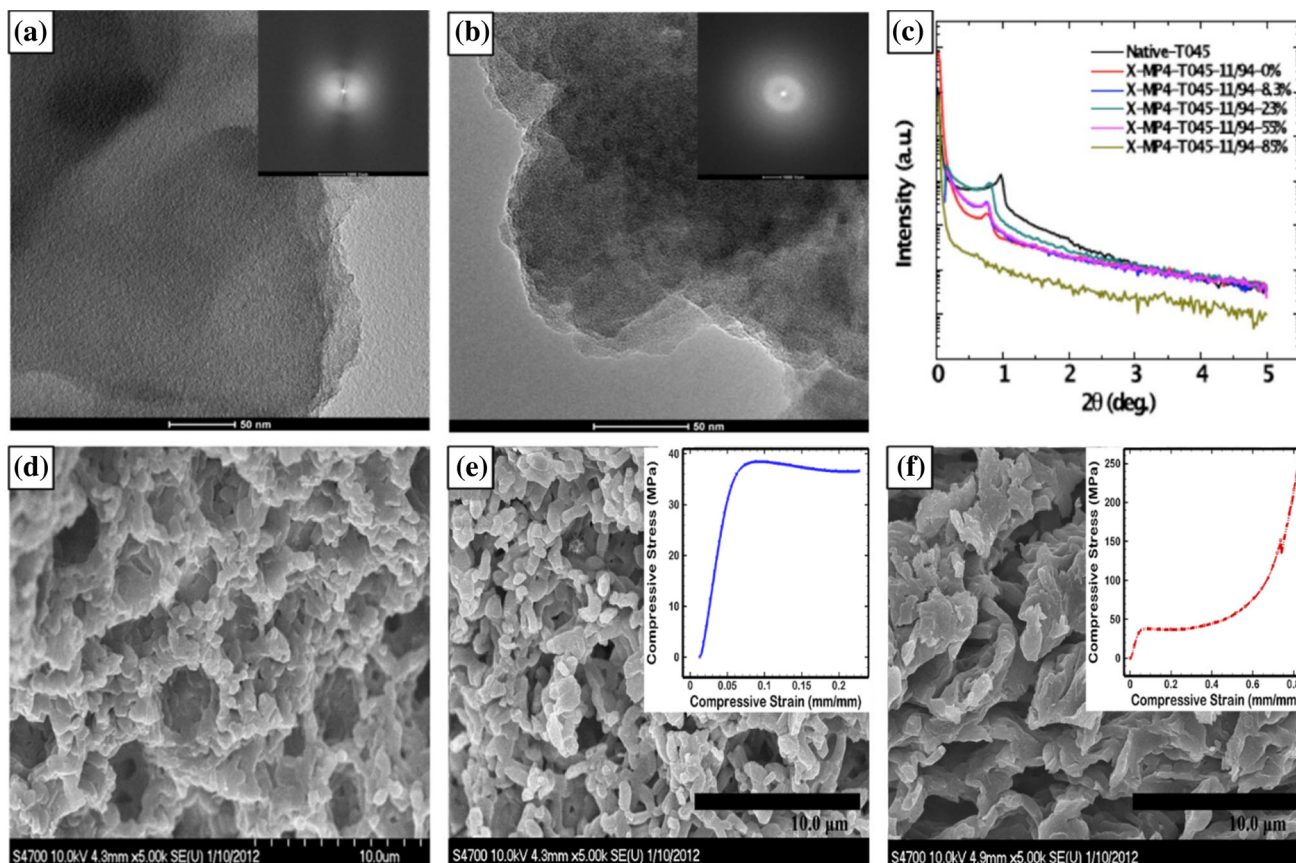
✉ Nicholas Leventis  
leventis@mst.edu

✉ Hongbing Lu  
hongbing.lu@utdallas.edu

<sup>1</sup> Department of Mechanical Engineering, The University of Texas at Dallas, Richardson, TX 75080, USA

<sup>2</sup> Center for Experimental Mechanics, University of Ljubljana, Pot za Brdom 104, 1125 Ljubljana, Slovenia

<sup>3</sup> Department of Chemistry, Missouri University of Science and Technology, Rolla, MO 65409, USA



TEM/SEM images and SAXS of X-MP4-T045-11/94 templated aerogel. (a) TEM images before compression; (b) TEM images after 85 % compressive strain; (c) SAXS data at different strain. (d) SEM images before compression; (e) SEM images after 23 % strain; (f) SEM images after 83 % strain. Insets of (e) and (f) are the compressive stress-strain curves.

**Keywords** Sol-gel · Silica · Crosslinked aerogels · Ambient drying · Supercritical drying · Mesoporous · Macroporous

## 1 Introduction

Aerogels are multifunctional, typically random fractal mesoporous materials [1–3] with low density, low thermal conductivity, low dielectric constant and high acoustic impedance. Those properties are attractive for a wide range of applications in thermal and acoustic insulation, electronics, separations [4], catalysts and catalyst supports [3], scaffolds for tissue engineering applications [5, 6] as well as platforms for drug delivery. The most common type of aerogels are based on silica. However, their

inherent fragility, hydrophilicity and the requirement for drying from supercritical fluids (e.g., SCF CO<sub>2</sub>) have limited their use to controlled/specialized environments. Thus, not surprising, the most well-established application is for thermal insulation of planetary vehicles in the dry environment of Mars. The fragility issue has been overcome successfully by nanoencapsulation of the entire skeletal framework with a thin (2–10 nm) layer of a conformal polymer layer [7–9], that bonds covalently and bridges skeletal silica nanoparticles. That polymer coating may increase the bulk density by up to a factor of three, but, importantly, it also reinforces the inter-particle necks, which are the weak points of the nanostructure, acting as stress concentrators. That crosslinking process furnishes materials whose flexural strength may be up to 300 times higher than that of the native (non-crosslinked) materials [7–10]. Meanwhile, the porosity is preserved, and consequently, the thermal and acoustic insulation capabilities have remained high. Importantly, polymer nanoencapsulation may reinforce the skeletal framework to the point where it can withstand the capillary forces exerted around the receding meniscus of evaporating low vapor pressure solvents (e.g., pentane) [9], allowing drying under ambient pressure.

More recently, those concepts have been applied to polymer (polyurea)-crosslinked, surfactant-templated silica aerogels (CTSAs). Those materials are similar to silicas first developed by Mobil Corporation in 1992 and have been referred to as M41S [11–13]. Their characteristic feature is their ordered (rather than random) mesoporosity comprising of uniformly spaced and sized nanotubes with large surface areas [12]. Typically, the diameters of those tubular mesopores are in the 2–3 nm range and are created with micelles of cationic surfactants acting as (soft) templates during gelation. Subsequently, Stucky [13] utilized large block copolymers (Pluronic 123) as templates, yielding materials referred to as SBAs with tubular pore sizes up to 30 nm. Addition of 1,3,5-trimethylbenzene (TMB) as a micelle-swelling agent increased the pore diameter further. In a modification of that method, Amatani et al. [14–16] developed monolithic (as opposed to powders) macroporous silica, whose macroporous walls were perforated by ordered mesoporous hexagonal tubes. Increasing the amount of TMB resulted in random meso/macroporous materials referred to as mesoporous cellular foams (MCFs). According to Amatani et al., the surfactant was removed by calcination of air-dried samples. However, we encountered difficulties when we attempted to apply that method in order to produce materials suitable for crosslinking and mechanical testing. The main problem was that air-drying of wet gels before removal of the surfactants resulted in large chunks rather than monoliths. Monoliths were obtained by removing the templating agent with Soxhlet extraction [17, 18]. Subsequent crosslinking with polyurea proceeded uneventfully, yielding extremely strong materials under quasi-static compression. Specific energy absorption values were found to be up to 123 J/g far surpassing those of other materials that are considered tough.

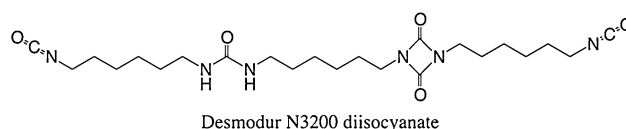
Based on those results, here we explore the properties of those materials as a function of the nanostructure by varying the amount of the swelling agent (TMB), and the concentration of the monomer precursor of the crosslinking polymer in the crosslinking bath. From a ballistic protection perspective, the mechanical behavior of interest includes quasi-static compression under low-strain-rate and high-strain-rate dynamic impact tests, tensile tests, shear creep tests as well as dynamic mechanical analysis (DMA). From a multifunctionality perspective, we also investigate the thermal conductivity as a function of structure and density.

## 2 Experimental section

### 2.1 Materials

All chemicals were obtained from readily available commercial sources and used as received without any further

processing unless noted otherwise. Nitric acid was purchased from Fisher Chemicals/Fisher Scientific (Pittsburgh, PA, 15275). Pluronic P123 (triblock copolymer: PEO<sub>20</sub> PPO<sub>70</sub> PEO<sub>20</sub>) and tetramethyl orthosilicate (TMOS) were purchased from Sigma-Aldrich Inc (St. Louis, MO, 63103), while TMB was purchased from Acros Organic ([www.acros.com](http://www.acros.com)). HPLC-grade acetone, 200 proof grain alcohol, HPLC-grade pentane and HPLC-grade acetonitrile (CH<sub>3</sub> CN) were purchased from Pharmco-AAPER Chemicals and Commercial Alcohols (Shelbyville, KY, 40065). Research samples of hexamethylene-1, 6-diisocyanate (Desmodur N3200) used for crosslinking were donated generously by Bayer Corporation USA (Pittsburgh, PA, 15205). Aluminum foil used to cover the molds was sourced from Reynolds Consumer Products Inc. (supplied locally by Walmart, [www.walmart.com](http://www.walmart.com)).



Plastic syringes (10 ml) used as molds for the cylindrical compressive samples were purchased from BD Syringes (Franklin Lakes, NJ, 07417).

To ensure compliance with ASTM standards, cylindrical specimens were machined with a lathe using a high-speed steel tool to the desired shape and size. Instron 5580 Testing System with a 50-kN load cell was used for quasi-static compression tests as well as tension tests. A convection Blue M temperature chamber ([www.thermo.com](http://www.thermo.com)) was used for gelling, aging and curing the samples as well as drying from pentane. Soxhlet extraction was conducted with a custom-made apparatus made by L&R Scientific Glass (Ponca City, OK 74602).

### 2.2 Synthesis of templated silica wet gels

The general protocol for preparing CTSA was similar to our previously published work [17], a modification of Amatani's work. In brief, Pluronic P123 (4.0 g) was dissolved in 1.0 M HNO<sub>3</sub> (12.0 g) under magnetic stirring. Depending on the desired morphology of the CTSA, different amount of TMB was added and the mixture was stirred for 30 min at room temperature. To mitigate the effect of the exothermic reaction with TMOS, the solution was cooled to 0 °C under vigorous stirring for 30 min, and then, TMOS (5.15 g) was added. After stirring for about 10 min, the solution was poured into suitable molds (e.g., 10-ml syringes for cylindrical samples used for quasi-static compression tests or rectangular plastic tabs used to make flat plates for dog-bone tensile samples).

The molds were covered by aluminum foil that was tightly molded on the mouth of the molds and were subsequently placed in the convection temperature chamber set at 60 °C for gelation and aging. In that regard, no shrinkage or unevenness in the shape of the gels was detected that could be attributed to escape of solvent from the top of the syringe molds since the aluminum foil provided a tight sealing. The samples were monitored every 10–15 min in order to determine the gelation times, and the aging time was set at 5× the gelation time at 60 °C. After aging, wet gels were removed from the molds and washed two times with ethyl alcohol, at 8-h interval each time, to remove gelation water. Subsequently, wet gels were subjected to Soxhlet extraction with acetonitrile for 36 h to remove the structure-directing agent (Pluronic P123). Next, wet gels were solvent-exchanged with acetone using 4–5 times of the volume of each gel (4 washes in 8 h intervals) and were either dried from CO<sub>2</sub> taken out as a supercritical fluid (SCF), or crosslinked with isocyanate-derived polyurea as described below.

### 2.3 Crosslinking and drying: crosslinked templated silica aerogels (CTSAs)

Unless noted otherwise, the crosslinking solution consisted of 11 g of Desmodur N3200 dissolved in 94 mL of dry acetone. The resulting samples are denoted as “11/94.” Other samples were made similarly and are noted as “32/82,” “23/88,” “5.5/94” and “16/82” [corresponding to the ratio of Desmodur N3200 (g) to the volume of acetone (mL) in the crosslinking bath]. Thus, wet gels after Soxhlet extraction and solvent exchange with acetone were placed in 4.5× their volume of the above solutions, and they were kept there for 36 h on a rocking platform shaker ([www.vwr.com](http://www.vwr.com)) for equilibration. Subsequently, samples were submerged in the above solution and were placed in a convection oven at 55 °C for 3 days. At the end of that period, unreacted Desmodur N3200 was washed off with four acetone washes (8 h per wash; for each wash, the amount of acetone was 4.5× the volume of the corresponding wet gel). At that point, acetone-filled wet gels were either dried in an autoclave with liquid CO<sub>2</sub> taken out at the end as a SCF, or they were further solvent-exchanged with pentane (four washes, 8 h per wash, using pentane that was 4.5× the volume of each wet gel). Drying from pentane involved first heating in the last pentane wash solution at 40 °C for 4 h followed by removal from the pentane wash container, placing in a preheated pan (also at 40 °C in the same oven) and further heating for 4 more h at 40 °C under atmospheric pressure. Control experiments were conducted by heating pentane-filled wet gels for 50 h at 50 °C, and the density of resulting aerogels was found to be equal to that of samples heated for 4 h at 40 °C.

### 2.4 General materials characterization

Bulk densities ( $\rho_b$ ) were determined from the weight and the physical dimensions of the samples. Skeletal densities ( $\rho_s$ ) were determined with helium pycnometry, using a Micromeritics AccuPyc II 1340 instrument. Porosities,  $\Pi$ , were determined from  $\rho_b$  and  $\rho_s$  according to  $\Pi = 100 \times [(\rho_s - \rho_b)/\rho_s]$ . Surface areas and mesopore size distributions were measured with N<sub>2</sub> sorption porosimetry, using a Micromeritics ASAP 2020 surface area and porosity analyzer. Samples for surface area and skeletal density determination were outgassed for 24 h at 80 °C under vacuum before analysis. Average pore diameters were determined by the  $4 \times V_{\text{Total}}/\sigma$  method, where  $V_{\text{Total}}$  is the total pore volume per gram of sample and  $\sigma$ , the surface area, was determined by the Brunauer–Emmett–Teller (BET) method.  $V_{\text{Total}}$  can be calculated either from the single highest volume of N<sub>2</sub> adsorbed along the adsorption isotherm or from the relationship  $V_{\text{Total}} = (1/\rho_b) - (1/\rho_s)$ . Macropore size distributions were determined with Hg-intrusion porosimetry using a Micromeritics AutoPore IV model 9500 instrument operated in the intrusion-only/set-time equilibration (10 s) mode. Pore sizes were calculated with the Washburn equation assuming cylindrical pores. Plotting the logarithmic differential intrusion volume ( $V$ ) versus pore diameter ( $D$ ) ( $dV/d \log D$  vs.  $D$ ) gives information about the average pore size and pore size distribution.

Heat capacities,  $c_p$ , at 23 °C of powders (4–8 mg), needed for the determination of their thermal conductivity,  $\lambda$ , were measured using a modulated differential scanning calorimeter (MDSC) calibrated using a sapphire standard and run from 0 to 40 °C at 0.5 °C·min<sup>-1</sup> in the modulated T4P mode, using 100 s as the modulation period and 0.13 °C as the modulation amplitude. Raw  $c_p$  data were multiplied by a factor of  $1.10 \pm 0.014$  based on measuring the heat capacities of rutile and graphite just before running the aerogel samples and comparing the results with literature values. Thermal diffusivity,  $R$ , was determined with a Netzsch Nanoflash model LFA 447 flash diffusivity instrument using disk samples ~1 cm in diameter, 1.8–2.5 mm thick. Samples were coated on both sides with gold and carbon to ensure the absorption of the heat pulse and to minimize radiated pathways and pulse “bleed through.” Before every run, the instrument reliability was confirmed with the standards provided by the manufacturer (Pyrex 7740, Pyrocera 9606, 99.8 % Alumina and AXM-5Q Poco Graphite).

Scanning electron microscopy (SEM) was conducted with Au-coated samples on a Hitachi model S-4700 field-emission microscope, while transmission electron microscopy (TEM) was conducted with a FEI Tecnai F20 instrument employing a Schottky field-emission filament

operating at a 200 kV accelerating voltage. For TEM, samples were ground to fine powders by hand in a mortar with a pestle; the smallest particles were selected and placed on a 200-mesh copper grid bearing a lacey Formvar/carbon film for microscopy. At least six (6) different areas/particles were examined on each sample to ensure that the results were representative of the material.

The structure of the fundamental building blocks of the materials and the  $d$ -spacing between regular hexagonal tubular structures were probed with small-angle X-ray scattering (SAXS), using 2- to 3-mm-thick disks with 7–10 mm diameter. SAXS was carried out with a PANalytical X'Pert Pro multipurpose diffractometer (MPD), configured for SAXS using Cu  $K\alpha$  radiation ( $\lambda = 1.54 \text{ \AA}$ ), a  $1/32^\circ$  SAXS slit, a  $1/16^\circ$  anti-scatter slit on the incident beam side, 0.1 mm anti-scatter slit and a 0.125-mm Ni automatic beam attenuator on the diffracted beam side. The samples were placed in circular holders between thin Mylar<sup>TM</sup> sheets. Scattering intensities were measured with a point detector in transmission geometry by 2 Theta scans ranging from  $0.1^\circ$  up to  $5^\circ$ . All scattering data are reported in arbitrary units as a function of 2 Theta.

## 2.5 Mechanical characterization

### 2.5.1 Quasi-static compression

Quasi-static compression was conducted to measure the basic mechanical properties of the materials such as the Young's modulus, yield strength, ultimate strength, Poisson's ratio and specific energy absorption. Physically, CTSA behaves very similar to rigid plastic foams, presumably due to the conformal polymer coating, and since there are no standard testing methods for aerogels, ASTM standard D695-10, which is equivalent to ISO 604, was employed. ASTM D695-10 is a standard for plastics and was chosen over a standard for plastic foams, because the standard for testing plastic foams requires large samples, which were much more difficult to prepare than the smaller samples specified in the standard for plastics. It is noted that testing of plastic foams requires large samples, because of the typical small-scale inhomogeneity in those materials. Aerogels prepared in this work have pore sizes on the order of a few  $\mu\text{m}$ , and the representative volume element has a side length on the order of ten times of the pore size; therefore, small samples are able to represent the mechanical behavior of the material adequately and thus large samples are not necessary for the determination of the basic mechanical properties. ASTM standard D695-10 uses cylindrical samples with length to diameter ratio of 2:1. Specimens were first machined to ensure size compliance with the ASTM standard. Subsequently, a fine-grade sandpaper (#600) was used to polish all surfaces of the

samples, to achieve a few  $\mu\text{m}$  surface roughness mainly to ensure that specimens had no surface scratches and cracks that would act as stress concentrators that might affect the reliability and reproducibility of the data. The final cylindrical compression specimens were 12.70 mm in diameter and 25.40 mm in length.

An Instron screw-driven testing 5580 system was used for testing at strain rates in the range of  $10^{-3} \sim 1.0 \text{ s}^{-1}$ . The strain rate was computed from the ratio of the crosshead speed of the machine and the gage length of the samples. The recorded force divided by the initial cross-sectional area was used to determine the nominal compressive stress. The recorded displacement was corrected for compliance of the test system by compressing two platens directly; and the corrected displacement divided by the initial length of the specimen was used to determine the nominal compressive strain. Quasi-static testing was conducted at room temperature and also under moist conditions as well as low temperatures. For compression at cryogenic temperatures, specimens were wrapped in aluminum foil and were immersed in liquid nitrogen in a Dewar flask for 24 h before testing. An Omega CY7-SD7 cryogenic silicon diode sensor was attached to the specimen surface, and an Omega CYC-320 thermometer was used to measure the actual surface temperature. During testing, liquid  $\text{N}_2$  was poured continuously over the samples to maintain a specimen surface temperature at  $-180^\circ\text{C}$  inside a thermally insulated foam chamber. The temperature was monitored continuously during testing, and the compression test was completed within 10 s by using a crosshead speed of 10 mm/s. All other test conditions were kept the same as those used for room temperature testing. The ambient temperature was measured as  $23 \pm 1^\circ\text{C}$  and the relative humidity was  $26 \pm 3\%$ , all within specifications of the ASTM D695-10 standards.

The effect of water on the mechanical properties of the materials was investigated by submerging specimens in water for 30 days. The bulk density of the wet specimens was monitored every 8 h for the first 2 days and then in 2-day intervals until there was no significant change in both the dimensions and weight of the specimens. For the dry specimens, tests were also carried out at different strain rates ranging from  $10^{-3}$  to  $1 \text{ s}^{-1}$ . In addition, some specimens were subjected to a series of loading and unloading in compression tests to evaluate incipient plastic deformations and the deformation recovery behavior.

A high-speed digital camera, XS-4 from IDT, was used to acquire images of a specimen coated with speckle pattern during compression at a frame rate of 3000 frames per second. Subsequently, the digital image correlation (DIC) technique [19–21], a non-contact full-field deformation measurement method, was used to measure the surface deformations. A speckle pattern with black silicone rubber

dots was created on the surface facing the camera in order to measure the local deformations and facilitate the measurement of Poisson's ratios. Silicone rubber coating is a soft material, with a Young's modulus of about 1 MPa, so that its strengthening effect is negligible. Prior to that, it was also determined that silicone does not react chemically with the materials of templated aerogels. In DIC, two images with locally distinct grayscale patterns representing the reference and the deformed states are compared to determine the surface deformations. In this work, the DIC algorithm developed by Lu and Cary [21], capable of measuring both first-order and second-order displacement gradients, was used to determine the strain fields in the specimens.

### 2.5.2 Dynamic mechanical analysis

Dynamic mechanical analysis (DMA) was conducted using rectangular beam specimens with dimensions of  $65 \times 13 \times 2$  mm cut from  $152 \times 76 \times 6$  mm plates. Samples were polished using fine-grade sandpaper (#600) and tested with a model RSA II dynamic mechanical analyzer (Rheometrics Scientific Inc., Piscataway, NJ) using a three-point bending fixture. Each sample was supported on the "knife" edges (48 mm span) in the test chamber, and a concentrated force was applied through a central knife edge at the mid-span to induce bending. A load of 0.10 N was introduced at the mid-span to ensure that the sample was always in contact with the knife-loading fixture when an oscillating load was applied. The frequency of the oscillating load was set at 1 Hz, and then, liquid nitrogen was introduced into the chamber to cool the sample down to the lower limit of  $-122$  °C; the upper temperature limit was set at 250 °C. The sample was soaked at  $-122$  °C for about 30 min to make sure that the material cooled to this temperature throughout its volume before starting the measurements. The temperature was then gradually increased at 4 °C/min. The storage modulus and loss modulus were measured, while the loss tangent was calculated.

### 2.5.3 Tensile testing

The use of pentane as a low vapor pressure solvent allowed us to dry aerogels in ambient conditions rather than using a supercritical drier, thus eliminating the size limitation imposed by the latter and allowed us to make larger aerogel pieces than those allowed by the autoclave used for conventional SCF drying before. According to ASTM standard D638-10 that is equivalent to ISO 527-1, rectangular aerogel samples with dimensions of  $165 \times 76 \times 6.5$  mm were prepared. The sol was poured into the mold sitting with its long side lying flat on the floor of the oven and tightly

covered with aluminum foil. Sols were allowed to gel and age in that position, resulting in wet gels at approximately the required dimensions ( $165 \text{ mm} \times 76 \text{ mm} \times 6.5 \text{ mm}$ , as mentioned above). Due to the large size of those wet gels, a large Soxhlet extractor (100 mm diameter, 280 mm tall) was custom-made by L&R Scientific Grass (Ponca City, OK 74602) and was used to remove Pluronic P123 as earlier mentioned. Once the samples were solvent-exchanged and dried from pentane, they were machined into Type II specimens as specified by the ASTM standard D638-10. Type II specimens were considered ideal for this work since a two-inch (50.8 mm) gage length extensometer could be used to accurately measure strain and consequently make accurate measurements of both the Young's modulus and 0.2 % yield point from the stress–strain curve. A commercially sourced Type II standard steel specimen (Laboratory Devices Company, [www.laboratorydevices.com](http://www.laboratorydevices.com)) was used to draw the outline of the dog-bone shape of the specimen, and then, a milling machine was used to cut out the samples. Subsequently, samples were polished with fine-grade sandpaper (#600) to remove any tool marks that would compromise the mechanical properties. Speckles were generated on the surface of the samples by placing a mesh over them and spraying black paint. The samples were then loaded on the tensile grips for testing by moving the top grip and simultaneously recording both the load and displacement while a 50.8-mm Instron extensometer was used to measure the strain. A high-speed camera was used to record images during deformation, which were analyzed using digital image correlation (DIC) technique. The speed of the tensile grip crosshead was set at 5 mm/min as specified by the ASTM standard.

### 2.5.4 Dynamic high-strain-rate compression

A modified long split Hopkinson pressure bar (SHPB) was used to characterize the high-strain rate behavior. Understanding the high-strain-rate mechanical behavior helps to evaluate the performance when the material is subjected to impact loading. Detailed setup of SHPB and the equations used to calculate stress, strain and strain rate are documented by Luo et al. [19, 20]. In brief, the SHPB setup consists of a steel striker bar launched by compressed air, an oscilloscope used to record the stress wave signals, a solid steel incident bar and a hollow steel transmission bar. The specimen was sandwiched between the incident and transmission bars. Copper disks were placed directly in front of incident bar as a pulse shapers to reduce dispersion of the incident wave and also to help reach dynamic stress equilibrium and establish a constant strain rate condition. Based on the Young's modulus determined from quasi-static compression tests, the wave speed through the samples was estimated to be about  $1000 \text{ m s}^{-1}$ , and this speed was used to estimate the time it takes for the wave to travel

across the specimen. Under valid experimental conditions indicated primarily by being able to achieve dynamic stress equilibrium and constant strain rate, the measured waves were analyzed to determine the stress–strain curves at high strain rates.

### 2.5.5 Shear creep measurements

The shear creep torsionmeter in the Centre for Experimental Mechanics at the University of Ljubljana was used for the measurement of shear creep compliance, which was documented in detail elsewhere [22–27]. In brief, the system consists of (a) a mechanical device enabling torsional loading of a test specimen in solid state, (b) a heating chamber and (c) a measurement and control station including a computer and software. All moving parts were equipped with aerostatic bearings to minimize friction. The smallest torque applied by the torsionmeter was  $3.2 \times 10^{-5}$  N m, and the angle of twist measurement range was from  $0^\circ$  to  $2.8^\circ$  with a resolution of  $0.005^\circ$ . The test specimen (12.7 mm in diameter and 36.0 mm in length) was placed in the heating chamber at several temperatures ranging from  $29 \pm 0.5$  to  $96 \pm 0.5$  °C. For testing, each cylindrical aerogel sample was fixed to metal holders using adhesives. CTSA samples were heated up from room temperature to 110 °C over a period of 3 h, were kept at that temperature for 4 h and then gradually cooled to 30 °C over a period of 8 h. The effects of physical aging were not considered in this work [27]. Next, testing was continued with loading, unloading and conditioning of the sample at various temperatures. The loading phase lasted for about 3 h at a constant temperature, then the loading torque was removed, and the temperature was increased. The process of heating took approximately 1 h, and then, the specimen was maintained at the new temperature for about 2 h. The specimen was again torque-loaded, and the procedure was repeated over the entire temperature range from 29 to 96 °C in intervals of approximately 10 °C. The actual temperature was measured with a thermocouple placed close to a specimen.

## 3 Results and discussion

### 3.1 Materials synthesis and the effectiveness of ambient pressure drying method

The synthesis procedure was essentially similar to the one described previously [17, 18], with the modification of ambient pressure drying from pentane-filled samples instead of SCF drying. Samples of variable morphology were synthesized by varying the amount of the micelle-swelling agent (TMB). Samples designated as MP4 were prepared

without TMB. Table 1 summarizes the TMB concentrations used for the various samples together with the gelation and aging times. The gelation time was found to be dependent on the amount of swelling agent that was added, and it decreased as the quantity of TMB in the sol increased. Physical properties were also dependent on the amount of swelling agent added as it determined the microstructure of the resulting gels. Thus, samples with medium concentrations of TMB (such as T045) had low percentage shrinkage well below 10 %, while samples with high concentrations of TMB had the highest shrinkage, perhaps due to formation of mesoporous microstructure.

Figure 1 shows the flow diagram of the preparation protocol. Because addition of TMOS in the 1 M HNO<sub>3</sub> solution of P123 and TMB is exothermic, the solution was cooled to 0 °C before addition of TMOS. After gelation and aging, most of the gelation water was removed with two washes with 200 proof ethanol. Subsequently, Soxhlet extraction with acetonitrile was used to remove P123. After Soxhlet extraction, samples were solvent-exchanged with acetone. Crosslinking with Desmodur N3200 was carried out in acetone. Once crosslinking was completed, samples were washed (solvent-exchanged) with acetone to remove unreacted N3200.

The innovation introduced in this work was the replacement of drying with SCF CO<sub>2</sub>, with ambient pressure drying [9]. That process has allowed preparation of samples without the size limitations imposed by the volume of common SCF dryers/autoclaves. More specifically, polymer-crosslinked and acetone-washed samples were solvent-exchanged with pentane and dried at 40 °C using a convection safety temperature chamber. The sample weight and dimensions were monitored and recorded in 30-min intervals for the first 4 h of drying. In order to evaluate the stability of the material, the oven temperature was raised to 50 °C, well above the boiling point of pentane (37 °C), and samples were left at that temperature for an additional 50 h; the mass and dimensions were measured every 2 h for the first 10 h and afterwards every 8 h. The mass of the pentane soaked samples decreased by 37.5 % during the first 2.5 h and stabilized after 4 h, while the volume decreased only by 1.3 % from the 4th to the 50th h, showing that the material had been stabilized in both mass and dimensions. Figure 2 shows the density, normalized mass and normalized volume of samples as a function of drying time. Clearly, the drying process was practically complete after 4 h at 40 °C, with no further significant changes in the mass or the sample dimensions even after 50 h at 50 °C.

For comparative analysis, some samples were also dried using the typical SCF method. Figure 3 shows SEM images of X-MP4-T045 and X-MP4-T090 dried with SCF- and pentane-dried samples. The micromorphologies of the samples within each SCF CO<sub>2</sub>-/pentane-dried pair are

**Table 1** Summary of composition and physical properties of templated silica aerogels

Sample	TMB (g)	Gelation/aging time (min)	Diameter (mm) <sup>c</sup>	Shrinkage (%) <sup>c,d</sup>	Bulk density (g/cm <sup>3</sup> )	Skeletal density (g/cm <sup>3</sup> ) <sup>e</sup>	Porosity (%)	BET surface area [avg. pore diam.] (m <sup>2</sup> g <sup>-1</sup> [nm] <sup>f</sup> )	Particle diam. (nm) <sup>g</sup>	<i>d</i> -spacing [ <i>z</i> <sub>0</sub> ] (Å [Å])
X-MP4	0	120/600	12.1 ± 0.0	13.4 ± 1.2	0.612 ± 0.121	1.335 ± 0.001	54	17.1 [11.8]	262.7	–
X-MP4-T010	0.10	117/585	11.8 ± 0.2	15.8 ± 2.6	0.63 ± 0.012	1.316 ± 0.003	52	1.81 [18.1]	2518.9	103 [118]
X-MP4-T030	0.30	113/565	12.8 ± 0.2	12.9 ± 1.9	0.65 ± 0.015	1.303 ± 0.001	50	1.63 [13.2]	2825.0	106 [123]
X-MP4-T045 <sup>a</sup>	0.45	110/550	12.6 ± 0.7	9.9 ± 0.1	0.675 ± 0.070	1.274 ± 0.002	47	1.61 [20.1]	2925.2	not done
X-MP4-T045 <sup>b</sup>	0.45	110/550	12.6 ± 0.9	9.7 ± 0.1	0.681 ± 0.004	1.276 ± 0.001	47	0.99 [300.3]	4751.1	115 [132]
X-MP4-T065	0.65	100/500	12.2 ± 0.2	12.6 ± 1.1	0.661 ± 0.023	1.291 ± 0.001	50	1.52 [50.8]	3068.2	116 [134]
X-MP4-T090 <sup>a</sup>	0.90	85/425	12.2 ± 0.1	13.0 ± 0.4	0.623 ± 0.024	1.307 ± 0.001	52	1.43 [81.4]	3211.2	not done
X-MP4-T090 <sup>b</sup>	0.90	85/425	12.2 ± 0.2	12.8 ± 0.8	0.732 ± 0.080	1.301 ± 0.000	51	1.40 [80.4]	3294.0	130 [150]
X-MP4-T125	1.25	75/375	12.0 ± 0.1	14.6 ± 0.1	0.632 ± 0.043	1.288 ± 0.000	66	5.01 [44.3]	929.9	<sup>h</sup>
X-MP4-T200	2.00	60/300	12.0 ± 0.0	14.6 ± 0.7	0.594 ± 0.026	1.290 ± 0.003	54	1.7 [50.7]	2735.5	<sup>h</sup>

Typically, 4 g of Pluronic P123 was dissolved in 12 g of a 1.0 M aq. HNO<sub>3</sub>; then 5.15 g of TMOS was added; samples were crosslinked in solution of Desmodur N3200 (11 g) dissolved in 94 ml of dry acetone

<sup>a</sup> SCF drying, <sup>b</sup> pentane drying, <sup>c</sup> average of four samples (mold diameter: 14 mm), <sup>d</sup> shrinkage = 100 × (sample diameter–mold diameter)/(mold diameter), <sup>e</sup> single sample, average of 50 measurements, <sup>f</sup> by the 4 × V<sub>Total</sub>/σ method. V<sub>Total</sub> was calculated by the single-point adsorption method, <sup>g</sup> calculated via  $r = 3/\rho_s\sigma$ , <sup>h</sup> no scattering peak detected

identical, and the bulk densities are equal to one another within experimental error. Similarly, Fig. 4 shows typical stress–strain curves under quasi-static compression (at a strain rate of 0.45 s<sup>-1</sup>) for polyurea-crosslinked X-MP4-T045 and X-MP4-T090 aerogels under unconfined conditions. The stress–strain curves for each pair of samples are either very close or nearly identical, confirming again that pentane-dried samples have the same mechanical behavior with that of the SCF-dried samples. By expanding the low strain range (Fig. 4—inset), the data from samples made using the two drying methods are 5 % from one another. Based on the similar structures and properties of the ambient dried samples and those from SCF CO<sub>2</sub>, ambient pressure dried samples are referred to as aerogels rather than xerogels. The most striking feature of those materials is their mechanical properties in conjunction with their microstructure, which becomes the focal point of Sect. 3.3 and beyond. Section 3.2 serves as a preamble, comprising a comparative overview of the general materials properties.

### 3.2 General materials characterization

General material properties are summarized in Table 1. The percent linear shrinkage of all aerogels relative to the dimensions of the molds is significantly higher in native samples than in their crosslinked counterparts. For example, native-MP4-T045 shrunk by 35 %, while the corresponding X-samples shrunk progressively less (Table 5), from 19 to 8 % as the Desmodur N3200 concentration in

the crosslinking baths increased from 5.5/94 to 32/82 (g/mL). On the other hand, for constant crosslinking bath concentration (11/94), the amount of swelling agent (TMB) used in the sol–gel synthesis does not appear to affect the extent of shrinkage, which seems to vary randomly from 10 to 16 % for X-samples that use from no TMB (denoted as X-MP4) to formulations with high concentrations of TMB such as those denoted as X-MP4-T200 (Table 1). Similarly, all bulk densities, ρ<sub>b</sub>, for X-samples from 11/94 bath formulations were found in the 0.6–0.7 g/cm<sup>3</sup> range. The skeletal density of native-MP4-T045 aerogels was 2.0 g/cm<sup>3</sup>, which is typical of amorphous silica, while all X-samples from the 11/94 bath formulation were about 1.3 g/cm<sup>3</sup>. The similar values of bulk and skeletal densities translate to similar porosities, which for all samples processed from 11/94 crosslinking baths were about 50 % v/v of empty space. For comparison, native-MP4-T045 samples were about 75 % v/v porous. Surface areas (by N<sub>2</sub> sorption porosimetry) were large for native samples (in the 550 m<sup>2</sup>/g range, Table 5) and generally much smaller in the X-samples. Pore diameters of the X-samples reveal some mesoporosity, but by the same token particle size calculations from the N<sub>2</sub> sorption data indicate very large (micron size) particles. The effects of the pore size and pore size distribution appear to have only minimal impact on the heat transfer characteristics of the resulting aerogels. According to Table 2, typical thermal conductivities, λ, were found to be in the range of 0.10–0.145 W m<sup>-1</sup> K<sup>-1</sup> and in one instance as low as 0.070 W m<sup>-1</sup> K<sup>-1</sup> for



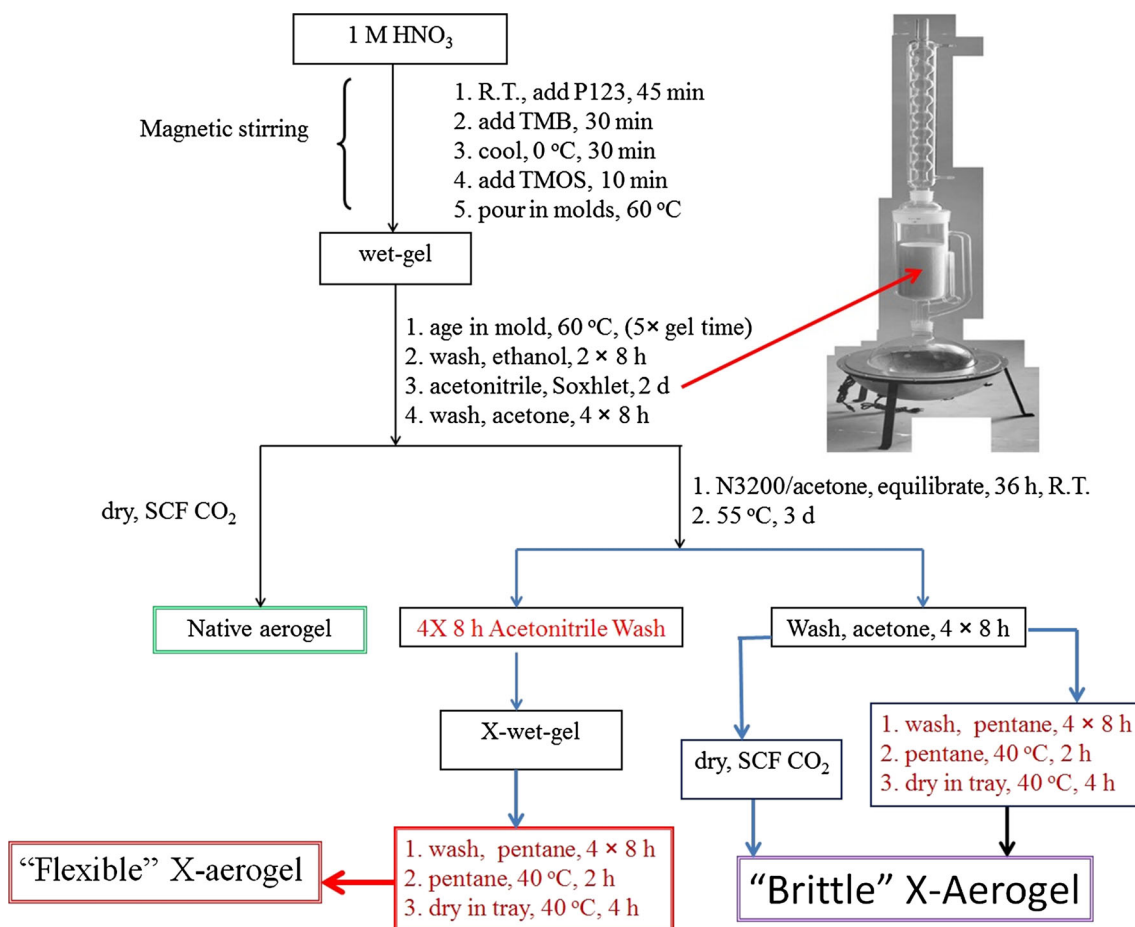


**Fig. 1** Flow chart for sample preparation of crosslinked templated silica aerogels

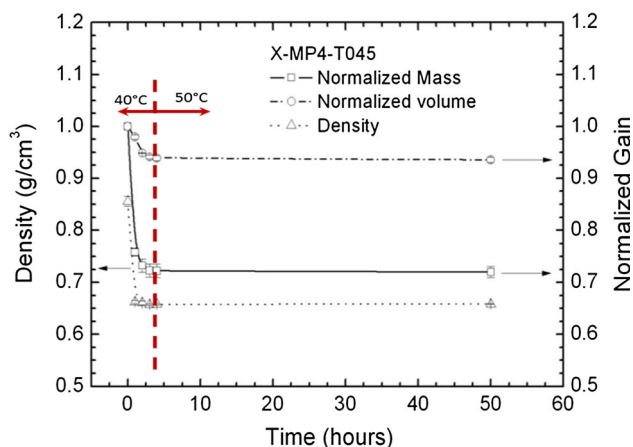


**Fig. 2** Density, normalized mass and normalized volume of X-MP4-T045 as a function of drying time during pentane drying process. Note: Left of the dashed line, drying was at 40 °C for 4 h, while right of the dashed line drying was at 50 °C for up to 50 h

X-MP4-T045-5.5/94, i.e., with the lowest crosslinker concentration and bulk density. Overall, thermal conductivities follow a direct relationship with the bulk density.

The contribution of the gaseous heat conduction,  $\lambda_g$ , was calculated using the Knudsen equation and is expected to be quite small, in the range of  $0.007\text{--}0.013\text{ W m}^{-1}\text{ K}^{-1}$ . Considering  $\lambda = \lambda_g + \lambda_s$ , the heat conduction through the solid network,  $\lambda_s$ , was identified as the main contributor to the total heat conduction. Assuming the usual exponential model between  $\lambda_s$  and  $\rho_b$  [ $\lambda_s = C(\rho_b)^a$ ], the pre-exponential factor,  $C$  (Table 2), is, within error, independent of the degree of crosslinking, meaning that the fundamental skeletal framework and interparticle connectivity is invariant of the crosslinking process.

SEM of representative native and crosslinked samples (Fig. 5) shows that the basic macroporous structure is generally preserved by crosslinking; however, there are some subtle differences. The most striking observation is that the microstructure of certain mid-range TMB native samples (T045) as well as the lightly crosslinked samples has a close resemblance to naturally occurring honeycomb structure—see Fig. 5b. The honeycomb-like microstructure may explain the remarkably better mechanical properties of this kind of samples [17] compared with other samples that had more random microstructure [10]. Even though

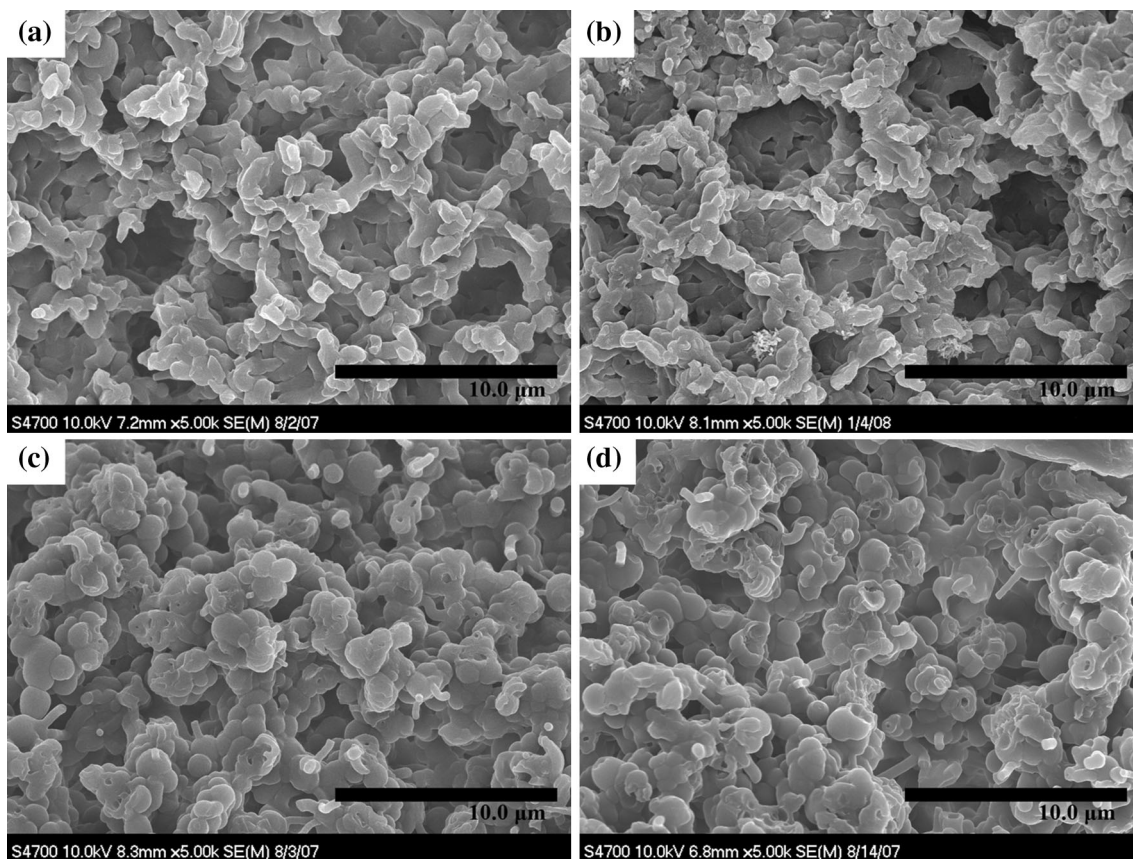


**Fig. 3** SEM images of templated aerogels comparing samples dried from pentane (left) with supercritical fluid (SCF)-dried samples (right). **a** Pentane-dried X-MP4-T045 ( $\rho_b = 0.71 \text{ g/cm}^3$ ). **b** SCF-

dried X-MP4-T045 ( $\rho_b = 0.71 \text{ g/cm}^3$ ). **c** Pentane-dried X-MP4-T090 ( $\rho_b = 0.74 \text{ g/cm}^3$ ). **d** SCF-dried X-MP4-T090 ( $\rho_b = 0.75 \text{ g/cm}^3$ ). Note:  $\rho_b$  is the bulk density

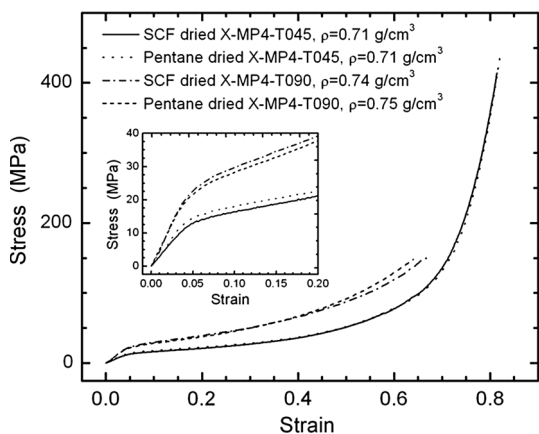


**Fig. 4** Quasi-static compressive stress–strain curves of templated silica aerogels dried from pentane and SCF. Inset: Zoomed-in view of the curve up to 20 % strain and 40 MPa stress

increasing the concentration of Desmodur N3200 in the crosslinking bath does have an effect on the bulk density (Table 1), it does not seem to have a significant effect on the wall thickness of the macropores, in agreement with the independence of the  $C$  values of the solid heat conduction

on the bulk density for constant skeletal frameworks (MP4-T030 and MP4-T045 samples). Therefore, the question is where is the polymer located?

TEM (Fig. 6) shows that the worm-like objects that define the macropores are hollow and may be perforated with parallel tubes. The tubes are clearly visible in the native samples, e.g., native-MP4-T045—Fig. 6a, but they are blurred in the X-samples—Fig. 6b, consistent with the small Z-attenuation between silica- and polymer-filling tubes, in agreement also with the dramatic reduction in surface areas (Table 1).

A quantitative view of the interior of the larger worm-like objects that form the macroporous network of the MP4-type samples, irrespective of whether they are filled with polymer, was obtained with SAXS (e.g., Figure 6d), and the results are summarized in Table 3. It is noted that the tube size in native samples is smaller ( $\alpha_o = 104 \text{ \AA}$ ) than the corresponding X-samples (123–138  $\text{\AA}$  for X-MP4-T045). This has been attributed to the fact that the polymer-filling tubes prevent shrinkage during the drying process. (It is noted in passing that yet polymer-filled tubes are under compression by the surrounding structure, which is

**Table 2** Heat transfer characteristics of crosslinked templated silica aerogels with varying concentrations of the swelling agent TMB

Sample	Bulk density, $\rho_b$ (g cm <sup>-3</sup> )	Heat capacity, $c_p$ (J g <sup>-1</sup> K <sup>-1</sup> )	Thermal diffusivity, $R$ (mm <sup>2</sup> s <sup>-1</sup> )	Thermal conductivity, $\lambda$ (W m <sup>-1</sup> K <sup>-1</sup> )	Gaseous thermal conductivity, $\lambda_g$ (W m <sup>-1</sup> K <sup>-1</sup> )	Solid thermal conductivity, $\lambda_s$ (W m <sup>-1</sup> K <sup>-1</sup> )	$C$ (W m <sup>-1</sup> K <sup>-1</sup> )
X-MP4-T010-11/94	0.63 ± 0.01	1.052 ± 0.063	0.168 ± 0.005	0.111 ± 0.001	0.0130	0.0980	0.1923
X-MP4-T030-11/94	0.65 ± 0.02	1.059 ± 0.045	0.152 ± 0.002	0.105 ± 0.001	0.0100	0.0950	0.1747
X-MP4-T045-32/82	0.85 ± 0.03	1.068 ± 0.096	0.162 ± 0.002	0.147 ± 0.014	0.0055	0.1415	0.1768
X-MP4-T045-23/88	0.80 ± 0.02	0.989 ± 0.074	0.145 ± 0.004	0.115 ± 0.001	0.0069	0.1081	0.1570
X-MP4-T045-12/88	0.73 ± 0.02	1.097 ± 0.048	0.161 ± 0.003	0.129 ± 0.001	0.0050	0.1240	0.2140
X-MP4-T045-11/94	0.68 ± 0.00	1.011 ± 0.103	0.154 ± 0.006	0.106 ± 0.001	0.0075	0.0985	0.1674
X-MP4-T045-5.5/94	0.50 ± 0.00	0.965 ± 0.097	0.145 ± 0.003	0.070 ± 0.001	0.0109	0.0591	0.1576
X-MP4-T065-11/94	0.68 ± 0.01	1.202 ± 0.119	0.148 ± 0.001	0.121 ± 0.001	0.0093	0.1117	0.2050
X-MP4-T090-11/94	0.63 ± 0.01	1.166 ± 0.052	0.141 ± 0.010	0.104 ± 0.001	0.0083	0.0957	0.1510
X-MP4-T125-11/94	0.64 ± 0.02	1.127 ± 0.093	0.131 ± 0.001	0.094 ± 0.002	0.0084	0.0856	0.1287
X-MP4-T200-11/94	0.63 ± 0.02	1.185 ± 0.027	0.135 ± 0.001	0.100 ± 0.001	0.0110	0.0890	0.1601

MP4-T045 samples had varying degrees of crosslinking

destroyed by ball-milling the tubes spring back to a size (150 nm) close to that in the native wet gels (146 nm), see Table 3.) Conversely, filling tubes with polymer under the same conditions (i.e., the same concentration in the crosslinking bath, i.e., 11/94) yield X-samples with increasing tube size as the amount of the micelle-swelling agent, TMB, increases: from  $\alpha_0 = 118 \text{ \AA}$  in X-MP4-T010 samples to  $\alpha_0 = 150 \text{ \AA}$  in X-MP4-T090 samples (Table 3). However, that does not go forever; samples X-MP4-T125 and X-MP4-T200 show no tubular internal structure in TEM and give no scattering in SAXS. In those samples, TMB forms droplets in the aqueous sol that utilize the surfactant (P123) for their stabilization, thus tubes are not formed, and the resulting materials are referred to as MCFs.

### 3.3 Mechanical characterization

#### 3.3.1 Quasi-static compression: general observations

ASTM D695-10 standard was used as mentioned earlier to obtain compressive stress–strain curves such as the ones shown in Figs. 4 and 7. In general, the stress–strain curves had three stages: a linearly elastic region under small compressive strain (<4 %); a nonlinear regime with slight hardening until about 60 % compressive strain, where the curve rises rapidly as more pores are compacted; and densification and plastic hardening range from 60 to 80 % compressive strain where all the pores become small. Taking a close look at both X-MP4-T045 and X-MP4-T090 in Fig. 4 inset, the curve rises only slightly after the yield point at about 5 % strain, showing that the material was simply absorbed by its porosity. At this stage, there were no noticeable lateral changes in specimen dimensions. The specific energy absorption was calculated from the area

under the stress–strain curves divided by the bulk density and was found to be as high as 123 J/g for X-MP4-T045 under quasi-static loading. The value is 63 % more than that of X-MP4-T090, because the latter developed cracks after about 65 % compressive strain, while X-MP4-T045 was compressed all the way to 83 % compressive strain. Therefore, the area under the stress–strain curve representing the mechanical energy absorption was much larger than that of X-MP4-T090. During initial compression (elastic region), X-MP4-T045 samples did not expand much laterally. When compressed to about 10 % strain, the specimen recovered its initial dimensions once the load was removed. Indeed, when samples were compressed up to 15 % axial strain, they were found to recover to over 97 % of their original dimensions once the load was removed. Figure 10b and c shows the recovery in the microstructures corresponding to the stress–strain curves that are insets in the corresponding SEM images. These results indicate that X-MP4-T045-11/94 has nonlinear elastic behavior up to about 15 % strain. Compaction continued without much visible lateral expansion up to about 40 % strain when visible deformation was realized and the sample expanded further until about 60 % compressive strain. Inset of Fig. 7d shows typical X-MP4-T045 samples before (at left) and after compression testing (at right). At failure, despite the splitting of the sample and the development of numerous cracks emanating in the radial fashion, the outer layer of all crosslinked samples did not shatter into fragments, but instead remained as single pieces for all the samples crosslinked with 11 g of N3200 dissolved in 94 mL of acetone (designated as “11/94”), or higher concentration of N3200. The cracks started at 83 % strain and the sample was deemed to have failed. However, native (uncrosslinked) samples and partially crosslinked samples such as those crosslinked with 5.5 g of Desmodur

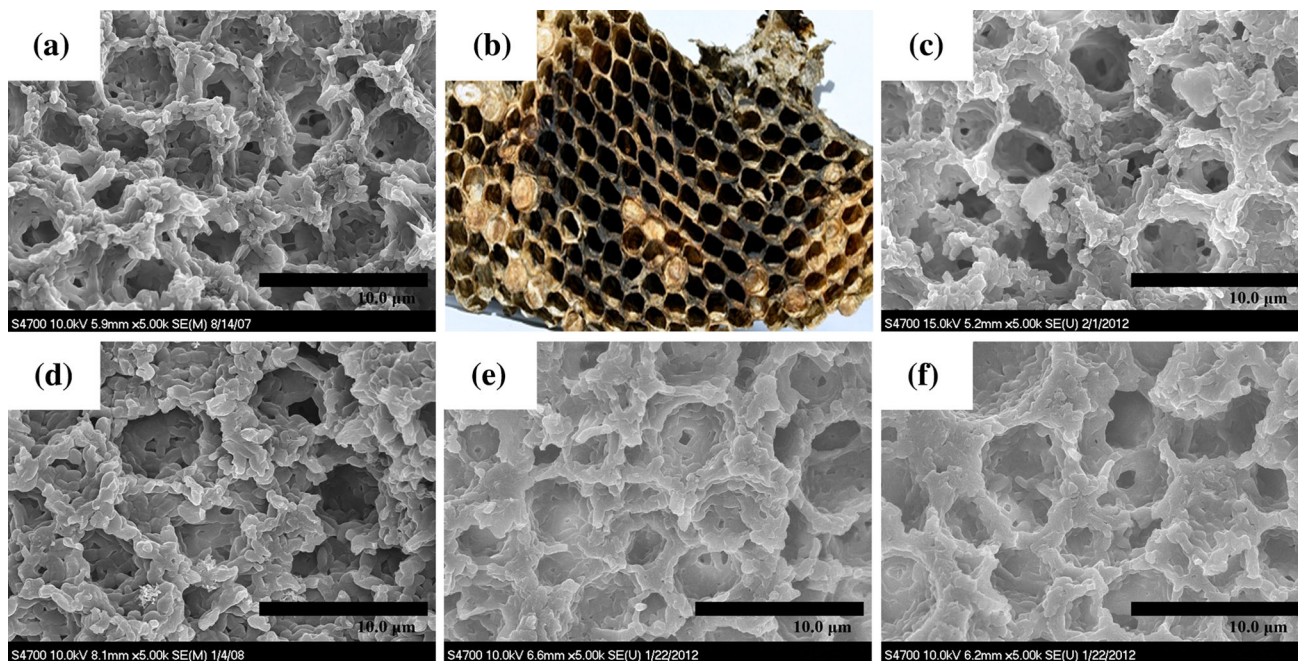


**Fig. 5** SEM images of X-MP4-T045 with varying amounts of crosslinking [N3200 (g)/Acetone (ml)]. **a** Native-MP4-T045. **b** Similar structure of honeycomb. **c** 5.5 g/94 ml. **d** 11 g/94 ml. **e** 23 g/88 ml. **f** 32 g/82 ml

**Fig. 6** TEM images and SAXS of templated aerogel. **a** TEM of native-MP4-T045 aerogel before compression. **b** TEM of X-MP4-T045-11/94 aerogel before compression. **c** TEM of X-MP4-T045-11/94 aerogel after 85 % compressive strain. **d** SAXS data of native and crosslinked templated silica aerogel at different levels of applied strain

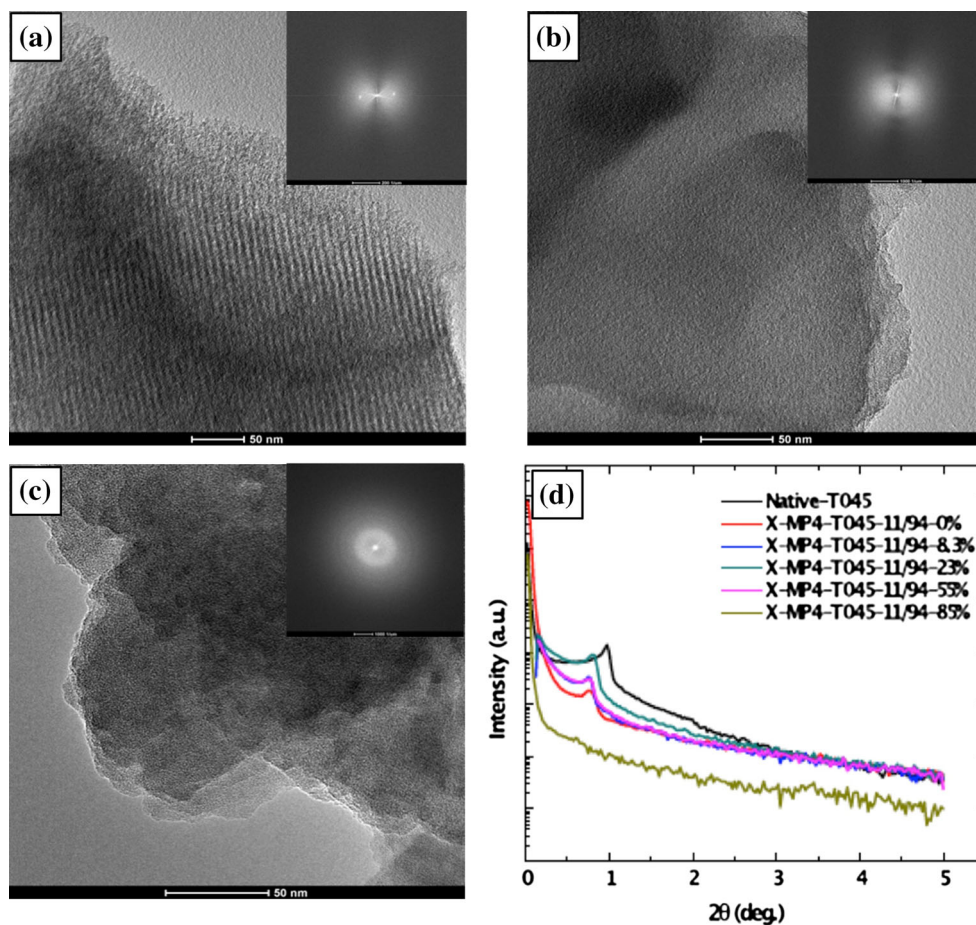


**Table 3** Structural characterization of surfactant-templated X-silica aerogels by SAXS after compression to different strains

Sample	<i>d</i> -spacing [ $\alpha_0$ ], (Å [Å]) at different compressive strains				
	Uncompressed	@ 7–10 % Strain	@ 23–30 % Strain	@ 54–60 % Strain	@ 65–85 % Strain
X-MP4-T010	103 [118]	109 [126]	110 [127]	116 [134]	Failed in the previous strain range
X-MP4-T030	106 [123]	115 [132]	Failed in the previous strain range		
Native-MP4-T045-wet gel	126 [146]	Not tested			
Native-MP4-T045	90 [104]	Not tested			
X-MP4-T045-5.5/94	106 [123]	106 [123]	Failed in the previous strain range		
X-MP4-T045	115 [132]	116 [134]	111 [128]	116 [134]	a
X-MP4-T045 (ball-milled)	130 [150]	N/A			
X-MP4-T045-12/88	118 [136]	116 [134]	120 [139]	121 [140]	a
X-MP4-T045-23/88	115 [132]	120 [139]	120 [139]	124 [144]	142 [164]
X-MP4-T045-32/82	119 [138]	119 [138]	118 [136]	124 [143]	163 [189]
X-MP4-T065	116 [134]	116 [134]	123 [142]	123 [142]	a
X-MP4-T090	130 [150]	134 [154]	134 [154]	134 [154]	a

All X-samples were of the –11/94 formulation, namely they were crosslinked with 11 g of Desmodur N3200 dissolved in 94 mL of dry acetone, unless noted explicitly otherwise (cases of X-MP4-T045 –5.5/94; –12/88; –23/88; –32/82). All samples were dried from pentane

<sup>a</sup> Failed in this strain range, but no SAXS pattern was observed

N3200 dissolved in 94 mL of acetone (denoted as “5.5/94”) had a brittle failure at less than 20 % strain. All quasi-static compression tests were conducted in the similar way, and the results are correlated with the preparation and sample treatment.

### 3.3.2 Effect of the micelle-swelling agent (TMB) on the structure and mechanical strength

TMB was used as a micelle-swelling reagent, to control the pore size and shape as well as the morphology. Samples designated as X-MP4 were prepared as control samples with no TMB. Gelation and aging times were found to depend on the concentration of TMB and decreased with increasing amount of TMB. Samples with no TMB took up to 2 h to gel while samples designated as MP4-T200, which used a high concentration of the swelling agent (TMB), took half that time. Figures 3 and 8 show SEM images of the morphology and the microstructure with varying amounts of the (TMB). The pore sizes are small and irregular, while secondary particles have a large degree of randomness for samples prepared without the swelling agent. In addition, they had lower porosity, with a relatively lower Young’s modulus and specific energy absorption as summarized in Table 4. As TMB concentration increased, the SEM images indicate that the microstructure became more ordered at low concentrations of TMB Table 5. Samples designated as X-MP4-T045 had regular and ordered pores (Figs. 3a, b) akin to the naturally occurring honeycomb structure shown in the inset of Fig. 5b, which are some of the most structurally optimized systems in nature. As a result, the mechanical properties are

significantly better for X-MP4-T045 than other specimens. As more TMB was added, the disorder in the pores increased from X-MP4-T065 to X-MP4-T090 to X-MP4-T125 and to X-MP4-T200, as shown in Fig. 8a–d, respectively. Higher concentrations of TMB resulted in samples with MCF characteristics, starting at about X-MP4-T125 to X-MP4-T310. Figure 9a shows the effect of TMB on the porosity, pore size as well as the BET surface area that confirms the results of the SEM images (Figs. 10, 3a, 5a).

The mechanical behavior of templated aerogel with various TMB concentrations was characterized under quasi-static compression at a strain rate of  $0.45 \text{ s}^{-1}$ . Compressive stress–strain curves with inset showing initial 25 % strain and 50 MPa stress range are presented in Fig. 7a. The characteristics of compression graphs are very similar, having three deformation stages as described earlier. The inset shows the main difference at elastic and initial plastic hardening stages. Samples with high TMB contents (X-MP4-T090, X-MP4-T125 and X-MP4-T200) had lower Young’s modulus as well as specific energy absorption (Table 4), as compared to X-MP4-T045 due to much more random and disorganized structure as shown in the SEMs in Figs. 3 and 8. Mechanical properties such as Young’s modulus ( $E$ ), proportional limit (0.2 % offset point) ( $\sigma_{0.2}$ ) and ultimate compressive strength ( $\sigma_b$ ) as determined from quasi-static tests are listed in Table 4. The Young’s modulus, proportional limit and density as a function of TMB contents are plotted in Fig. 9b. As TMB concentration increased, the density increased, until the point where 1.25 g of TMB was added and then decreased again with further addition of TMB, mainly due to the

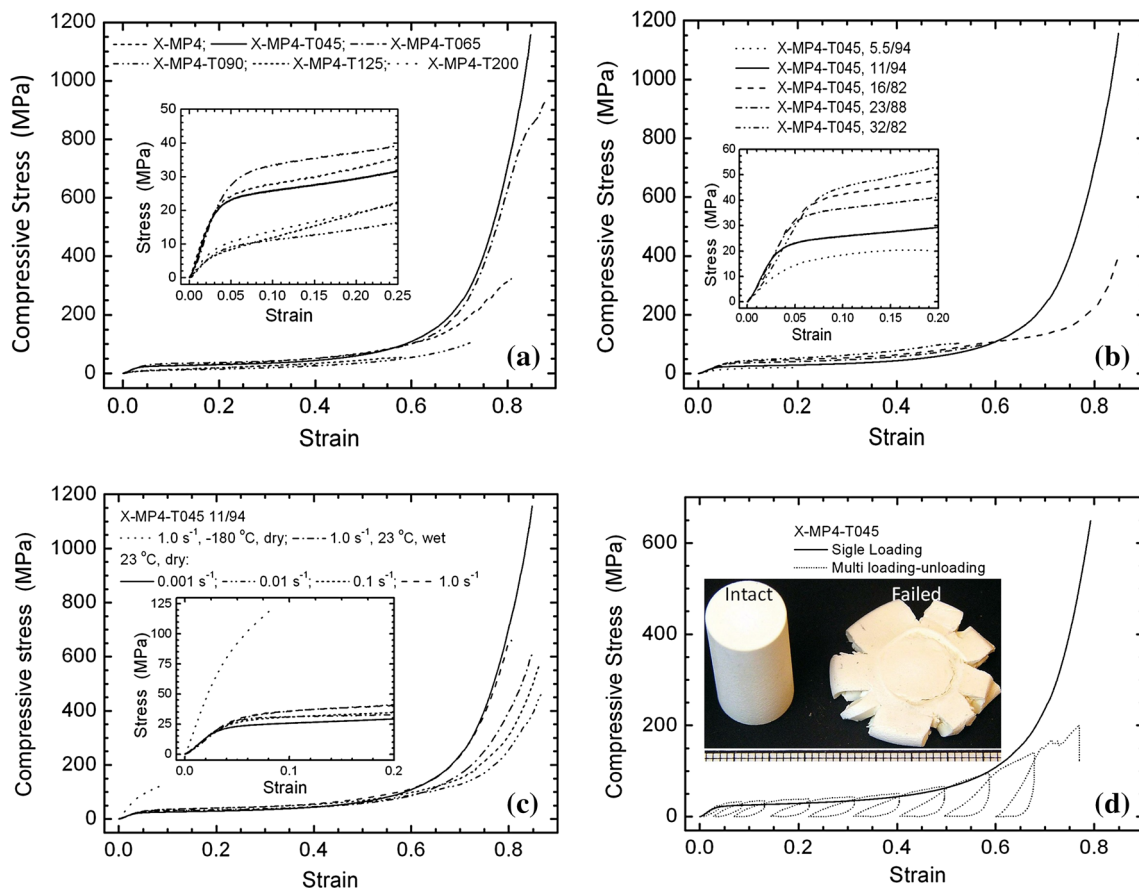


**Fig. 7** Quasi-static compressive stress–strain curve of templated silica aerogel. *Insets* in (a), (b) and (c) are zoomed-in views of the curves to show the initial elastic regime and up to 25 % strain and 50 MPa stress. **a** Effect of TMB concentration. **b** Effect of

crosslinking concentration. **c** Effects of cryogenic temperatures, moisture and changing strain rate. **d** Effect of loading–unloading. *Insert*: samples before (*left*) and after (*right*) quasi-static compression testing. The small grid on the *bottom* of rulers is in the scale of 1 mm

change in morphology from mesoporous to foam-like structure.

### 3.3.3 Effect of the extent of crosslinking on the mechanical properties

A solution of Desmodur N3200 dissolved in dry acetone was used to apply a conformal thin coating of polymer on the walls of the pores without clogging the pores. The concentration of N3200 was varied in order to adjust the thickness of the conformal polymer layer on the surface of the mesoporous walls and further change the microstructure and consequently the mechanical and physical properties of CTSA. Figure 5 shows SEM images of X-MP4-T045 with varying concentration of N3200 in acetone. As the concentration of N3200 increased, there was significant distortion in sample shape. Samples crosslinked in 23/88 and 32/82 (N3200/acetone ratio in g/mL) showed severe dimensional distortion after they were cured in the oven due to excessive polymer, which

partially blocked the pores. As a result, those samples had higher density and lower porosity as listed in Table 5. In addition, 32/82 samples formed distinct layers comprising of a whitish center core and a darker outer core, probably as a result of phase separation due to the fact that the polymer formation was faster than the rate at which the crosslinking solution diffused across the sample thickness. Thus, the reaction between the gel and the monomer occurred faster than the crosslinking monomer could diffuse through the sample’s entire thickness. The physical data such as BET surface area, porosity and average pore diameter are plotted in Fig. 9c as a function of N3200 concentration. BET surface area as well as porosity decreased with increased N3200 concentration mainly because the polymer layer on the mesopores increased and the walls of the pores became thicker and thus reduced the inner diameter of the pores at high concentration especially in the 23/88 and 32/82 (N3200/acetone ratio) samples which had more polymer coating.

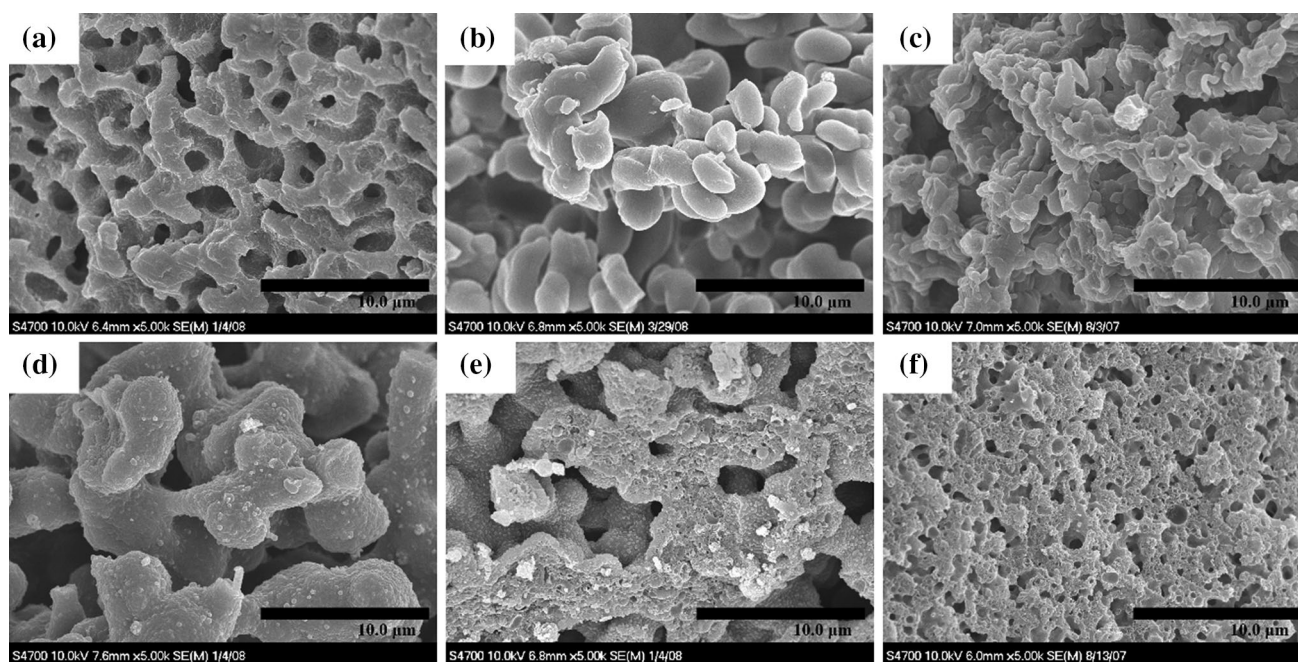


**Fig. 8** SEM images of X-MP4 samples with varying concentration of the swelling agent TMB. All samples were crosslinked with 11 g of N3200 dissolved in 94 ml of dry acetone. X-MP4 had no TMB. SEM

images for X-MP4-T045 and X-MP4-T90 samples are shown in Fig. 3. **a** X-MP4. **b** X-MP4-T030. **c** X-MP4-T065. **d** X-MP4-T125. **e** X-MP4-T200. **f** X-MP4-T310

**Table 4** Summary of mechanical properties under quasi-static compression (strain rate  $\sim 0.45 \text{ s}^{-1}$ ) of X-MP4 with varying concentrations of the swelling agent TMB

Sample	Bulk density (g/cm <sup>3</sup> )	Young's modulus, E (GPa)	Yield strength (MPa)	Ultimate strain (%)	Strain energy density (MPa. m/m)	Specific energy density (J/g)
X-MP4-T00	$0.612 \pm 0.121$	$0.621 \pm 0.154$	$15.94 \pm 0.69$	$63.10 \pm 0.00$	52.1	85.1
X-MP4-T010	$0.633 \pm 0.122$	$0.561 \pm 0.091$	$15.37 \pm 2.06$	$51.68 \pm 2.76$	14.1	22.2
X-MP4-T030	$0.652 \pm 0.014$	$0.440 \pm 0.023$	$13.78 \pm 0.28$	$10.00 \pm 2.64$	1.3	2.0
X-MP4-T045	$0.690 \pm 0.004$	$0.867 \pm 0.017$	$23.22 \pm 0.81$	$82.83 \pm 2.65$	84.3	122.2
X-MP4-T065	$0.682 \pm 0.008$	$0.854 \pm 0.031$	$21.08 \pm 1.30$	$80.96 \pm 0.00$	47.9	116.0
X-MP4-T085	$0.655 \pm 0.002$	$0.500 \pm 0.089$	$12.98 \pm 1.75$	$76.12 \pm 5.31$	66.5	101.5
X-MP4-T090	$0.732 \pm 0.080$	$0.628 \pm 0.110$	$14.67 \pm 0.82$	$72.79 \pm 9.20$	84.0	115.0
X-MP4-T125	$0.847 \pm 0.022$	$0.763 \pm 0.267$	$18.71 \pm 1.42$	$75.58 \pm 2.61$	100.0	123.0
X-MP4-T200	$0.660 \pm 0.002$	$0.379 \pm 0.026$	$9.43 \pm 0.50$	$42.34 \pm 2.19$	49.0	71.1

All samples were crosslinked with 11 g of N3200 dissolved in 94 ml of dry acetone and dried from pentane. Average of three samples

During quasi-static compression, all specimens showed a linear elastic regime up to about 5 % strain after which yielding occurred followed by compaction up to a compressive strain of about 60 %. Samples with high concentrations of N3200 failed by radial fracture while the more evenly crosslinked samples (X-MP4-T045, 11/94) were compressed up to 83 % strain before failure occurred (Fig. 7b). The inset shows the compressive stress–strain curves for the initial 20 % strain and 60 MPa stress range. The characteristics of compression curve are very similar, having three similar deformation stages. The inset also shows the main difference at elastic and initial plastic hardening stages. The mechanical properties such as

Young's modulus, yield strength and ultimate compressive strength as determined from Fig. 7b, are listed in Table 6. Samples crosslinked in 23/88 and 32/82 (N3200/acetone ratio) failed at less than 60 % strain mainly after the whitish core separated from the outer darker shell, while samples with 11/94 displayed uniform crosslinking whereby the polymer was equally distributed throughout the sample with no phase separation which occurred with highly crosslinked samples. It was therefore possible to compress them all the way to failure without cracking or separation to over 80 % strain. That was in contrast to samples with 5.5/94, which were weak and brittle and behaved more like their native counterparts, indicating that

**Table 5** Summary of physical properties for X-MP4-T045 crosslinked with varying concentrations of N3200 oligomer dissolved in dry acetone

N3200/acetone (g/ml)	Diameter (mm)	Shrinkage (%)	Bulk density (g/cm <sup>3</sup> )	Skeletal density (g/cm <sup>3</sup> )	Porosity (%)	BET surface area [Avg. pore dia.] (m <sup>2</sup> g <sup>-1</sup> [nm])	Particle diam. (nm)	<i>d</i> -spacing [ $\alpha_0$ ] (Å [Å]) <sup>b</sup>
0.0/0.0 <sup>a</sup>	9.08	35.2	0.477	1.965	76	556.1 [3.8]	5.4	90 [104]
5.5/94	11.33	19.1	0.496	1.377	64	155.9 [93.2]	27.9	106 [123]
11/94	12.60	10.0	0.681	1.276	47	0.99 [300.3]	4751.1	115 [132]
23/88	12.81	8.5	0.792	1.255	37	8.97 [21.9]	532.8	115 [132]
32/82	12.86	8.1	0.843	1.244	32	1.14 [25.5]	4231.8	119 [138]

<sup>a</sup> Native MP4-T045 without N3200; pentane-dried, mold used had 14 mm inner diameter

<sup>b</sup> *d*-spacing calculated for uncompressed samples

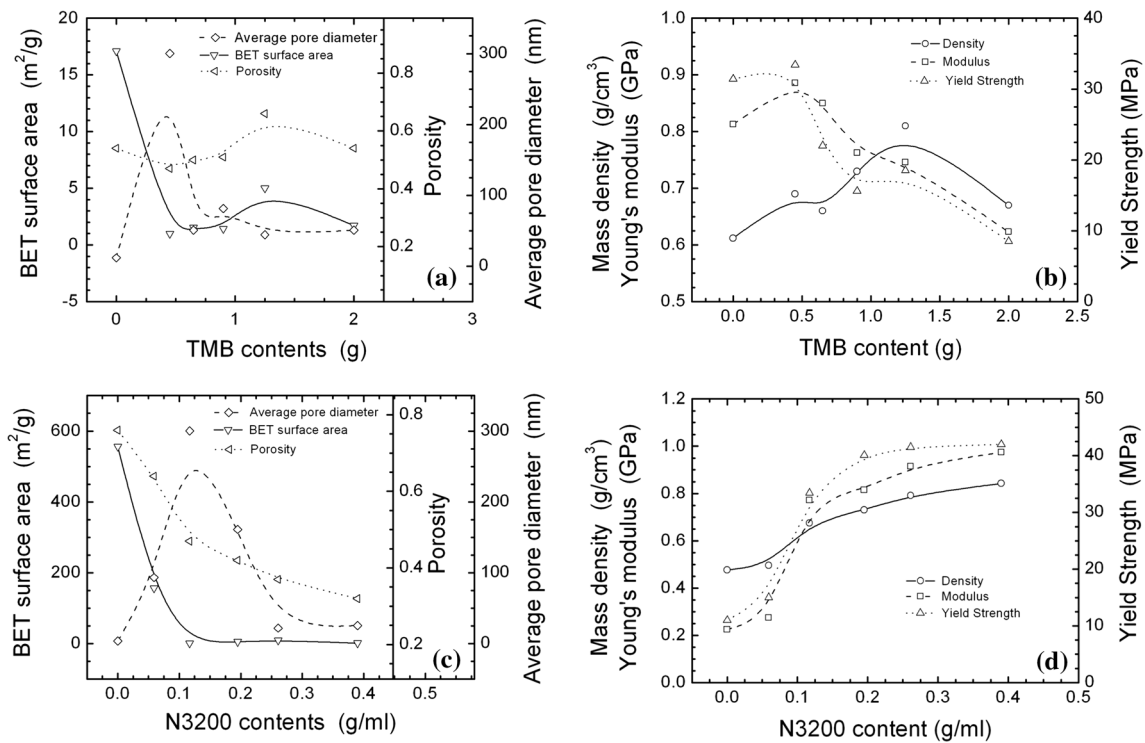


**Fig. 9** Physical, microstructural and mechanical properties of templated silica aerogels. **a** BET surface area, porosity and average pore diameter as a function of TMB concentration. **b** Density, Young's modulus and yield strength as a function of TMB concentration.

**c** BET surface area, porosity and average pore diameter as a function of N3200 concentration in acetone. **d** Density, Young's modulus and yield strength as a function of N3200 concentration in acetone

they were not fully crosslinked due to insufficient polymer in the dilute N3200 solution.

The Young's modulus, yield strength and density as a function of N3200 concentration are plotted in Fig. 9d along with the corresponding mass density. Results of the quasi-static compression showed that the yield strength and the Young's modulus increased with the increase in concentration of crosslinking agent N3200. Samples crosslinked with 32/82 had the highest yield strength, approaching what is expected of polyurea, while samples with 5.5/94 had the lowest yield strength among those

samples. In addition, 32/82 samples had the highest density, while samples with 5.5/94 had the lowest density among the crosslinked samples, and as in most aerogel materials, mechanical properties could be closely correlated with bulk density. When the optimum amount of crosslinking was applied (using 11 g of N3200 dissolved in 94 ml of dry acetone), the stiffness based on the calculated Young's modulus increased by a factor of four compared with native samples, while the ultimate compressive stress increased by a factor of 40. More significantly (Table 6), the specific energy absorption of the material increased by



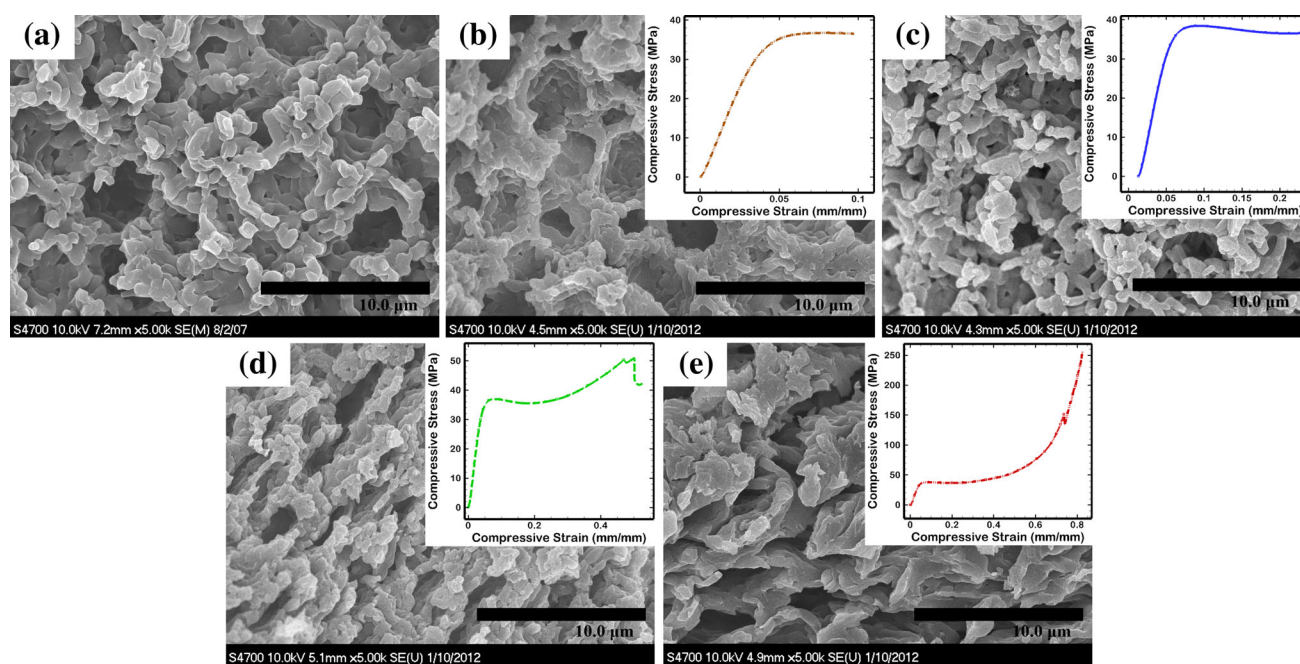


**Fig. 10** SEM images of the microstructure evolution of X-MP4-T45-11/94 during quasi-static compression test. *Insets* are the corresponding *stress–strain* curves from quasi-static compression tests at the

different strain level: **a** uncompressed, **b** 8 % compressive strain, **c** 23 % compressive strain, **d** 55 % compressive strain and **e** 83 % compressive strain

**Table 6** Summary of mechanical properties for X-MP4-T045 with varying degrees of crosslinking under quasi-static compression (strain rate  $\sim 0.45 \text{ s}^{-1}$ )

N3200/ Acetone (g/ml)	Bulk density (g/cm <sup>3</sup> )	Young's Modulus, E (GPa)	Yield strength (MPa)	Ultimate stress (MPa)	Ultimate strain (%)	Specific energy density (J/g)	<i>d</i> -spacing [ $\alpha_0$ ] (Å [Å]) <sup>b</sup>
MP4-T45 <sup>a</sup>	0.477 ± 0.000	0.205 ± 0.017	12.1	17.12	7.2	6.8	90 [104]
X-MP4-T45-5.5/94	0.535 ± 0.003	0.276 ± 0.002	15.6	153.7	15.3	2.15	106 [123]
X-MP4-T045-11/94	0.678 ± 0.007	0.867 ± 0.017	23.5	636 ± 252	85	187	–
X-MP4-T045-12/88	0.690 ± 0.004	0.691 ± 0.043	24.5	547.83	86.3	132.25	–
X-MP4-T045-16/82	0.729 ± 0.018	0.722 ± 0.039	29.0	216.79	82.5	90.44	–
X-MP4-T045-23/88	0.792 ± 0.051	0.754 ± 0.094	34.6	450.5 ± 105	79	36.1	142 [164]
X-MP4-T045-32/82	0.847 ± 0.029	0.915 ± 0.009	42.4	220.6 ± 32.0	72.6	48.7	163 [189]

<sup>a</sup> Native MP4-T045 was not crosslinked with N3200; all samples were dried from pentane

<sup>b</sup> *d*-spacing was calculated for uncompressed samples

a factor of about 25 while the bulk density increased by only 1.45 times from that of the native samples, implying a huge gain in mechanical strength with very small weight penalty for samples consisting of with X-MP4-T045 and crosslinked with the 11/94 formulation, as compared to native samples.

### 3.3.4 The effect of the strain rate on the mechanical properties under quasi-static compression

The effect of strain rate on the mechanical behavior was evaluated under quasi-static loading conditions. Figure 7c

shows the stress–strain curves at strain rates 0.001, 0.01, 0.1 and 1.0  $\text{s}^{-1}$  for X-MP4-T045. The inset shows the zoomed-in initial region of the curves at the strain range below 20 % compressive strain. As the strain rate increased by three orders of magnitude, Young's modulus and yield strength increased, shifting the curve upward, indicating that at these strain rates, the mechanical behavior for templated aerogel depends on the strain rate. In addition, the yield strength increased dramatically indicating that the material will be ideal for high impact applications to absorb and dissipate energy such as in case of bullet-proof plates. Further testing at high strain rates using a SHPB

would be necessary to study how the material responds to strain rate that is more than three orders of magnitude higher than what was applied during quasi-static compression tests.

### 3.3.5 Effect of water absorption on compressive strength

Hydrophilicity is one of the problems hindering widespread use of aerogels. Therefore, it was necessary to study the effect of water content on the mechanical properties of CTSA. In this study, samples were kept in water for 30 days before quasi-static compression tests were conducted. The weight and the dimensions of the samples were recorded before submerging them in water and then every 8 h for the first 3 days and subsequently every other day for 30 days. Initially, all the samples floated in water for 2 to 7 days depending on the amount of crosslinking as well as the amount of TMB in them. The partially crosslinked X-MP4-T045 (with N3200 to acetone ratio of 5.5/94) samples had the biggest open pores and were the first to sink with no visible sign of dissolving or disintegrating in water. Water was simply absorbed by the open pores, indicating a more robust open pore network that is strong enough and capable of withstanding the surface tension forces of liquid compared with native samples. The effect of water absorption on the mechanical properties was investigated by comparing compression data using both dry and water-soaked samples. After immersion in water for 30 days, samples reached fully saturated state, and the weight increased by 11.7 %, while their volume increased by an average of 5.1 %, indicating that water occupied the pores without significant changes in the network microstructure. Figure 7c also compares the stress–strain curves for both dry and water-soaked X-MP4-T045 samples at a strain rate of  $1.0 \text{ s}^{-1}$ . The inset shows the similarity of the initial stress–strain curve at low strain range. It can be concluded that the mechanical properties of water-soaked samples are only slightly lower than those of a dry sample. The Young's modulus, yield strength and ultimate compressive strength of water-soaked X-MP4-T045 decreased by 5.9, 16 and 6.1 %, respectively, compared with dry X-MP4-T045. But remarkably, the water-soaked samples were still stable, did not disintegrate in water and were still ductile, albeit not as much as the dry samples at the strain region larger than 50 % in the compressive stress–strain curve. The water-soaked samples failed at an ultimate compressive strength of 610 MPa at an ultimate compressive strain of 84 %, a little lower than that of the dry samples.

### 3.3.6 Effect of temperature on the strength under quasi-static compression

Figure 7c also shows compression results of X-MP4-T045 at cryogenic temperatures at a strain rate of  $1.0 \text{ s}^{-1}$ . As the temperature decreased, the material became brittle and stiffer, leading to a stress–strain curve that is shifted upwards, indicating that X-MP4-T045 can still absorb large amounts of energy at about  $-180 \text{ }^\circ\text{C}$ , similar to crosslinked vanadia aerogels [20]. The sample still remained relatively ductile with 8 % compressive strain and ultimately fractured and disintegrated.

### 3.3.7 Mechanical behavior under cyclic quasi-static loading and unloading

The ability of the material to handle repetitive loading and unloading cycles was conducted on standard ASTM D695-10 specimens. Figure 7d shows the stress–strain curve with nine loading–unloading–reloading cycles. The stress–strain curve traced slightly over that of the single continuous loading, indicating that the material became stronger after repetitive loading and then developed cracks at about 70 % strain. The loading curves traced almost parallel to that of single continuous compressive loading, showing that the material undergoes repetitive loading in a similar way. To some extent, samples became stiffer after each loading cycle and all unloading exhibited nonlinear recovery. At the beginning of each unloading part of the cycle, even though stress starts to decrease, the strain would keep increasing due to viscoelastic memory effect, resulting in a negative slope (stiffness) in the initial unloading stage of each cycle mainly due to the covalently bonded polymer coating. Reloading does not follow the unloading curves, resulting in a hysteresis loop in each unloading/reloading cycle. The unloading curve becomes steeper at higher compressive strain levels (e.g., between 68 and 76 %), showing a reduced elastic behavior for samples having experienced higher level of densification due to compaction from the preceding loading cycle. By comparison, samples having gone through multiple loading/unloading cycles are weaker than the single monotonic loading curve at high strain ( $>50 \%$ ) and stronger below the densification ( $<50 \%$ ). Again, this behavior is most likely due to the combined effect of the silica network microstructure and the viscoelastic effects induced by the polymer nanocoating, which results in a memory effect where the subsequent curve would be affected by the preceding unloading and be adjusted lower than the monotonic loading curve at strains higher than 50 %.

### 3.3.8 Materials characterization during and after compression

Materials were characterized along the way to the ultimate compressive strain in order to understand the mode of failure and help design better systems. Tables 3, 5, 7 and 8 summarize the effect of compression on the microstructure in terms of density and porosity. At the ultimate strain (Table 3), bulk densities have increased as compared to Table 1; on the other hand, skeletal densities have remained practically unchanged, meaning that the most basic building blocks of the material have not undergone any fundamental change. The percent of empty spaces (porosity) has consequently decreased, yet has still remained significant. As expected, materials that failed early (e.g., X-MP4-T030 at 8.6 % strain) retained most of the porosity (49 % v/v) because pores were not compressed or compromised by the applied loads. Samples simply shattered at low strain levels, and therefore, stress did not get a chance to build up to reach high levels.

A specific formulation (X-MP4-T045-11/94) was chosen in order to follow the effect of compression in detail along the way to the ultimate strain (Table 8). Data show a progressive decrease in porosity (from 44.6 % v/v for the uncompressed sample to 29 % v/v at the point of failure at 85 % strain). The skeletal density remained constant, while the bulk density increased from 0.7 to 0.9 g/cm<sup>3</sup>. It appears that the overall bulk density increase and porosity decrease are disproportional to the low magnitude of the ultimate stress. This dictates a closer observation at the evolution of microstructure. That was accomplished qualitatively with a combination of SEM and TEM, while the ultimate quantification of changes happening within the fundamental building blocks of the material during compression was obtained with SAXS.

Figure 10 shows the evolution of the microstructure during compression. Inset shows the corresponding stress–strain curves as a function of the degree of compression. SEM of X-MP4-T045 after ultimate compression (see Fig. 10e) shows that the honeycomb-like macroporous structure has been destroyed; however, the material still included irregular microporosity. A glimpse at the fate of the tubular microstructure inside the nanoworms that comprise the walls to defining the macropores was obtained with TEM (see Fig. 6). It appears that the tubular microstructure has disappeared, although as mentioned above, the low Z-attenuation difference between silica and the polymer makes the quantification quite difficult. On the other hand, SAXS overcomes this issue and provides an accurate picture of the evolution of the tubular microstructure upon compression. SAXS data for native and X-MP4-T045 samples along various stages of compressive strain are shown in Fig. 6d. SAXS results for all

crosslinked samples at various stages of compression along with key controls are summarized in Table 3.

A common observation for all samples tested is an expansion of the primary tubular nanostructure (wherever one is observed). In some types of samples (X-MP4-T10; X-MP4-T30; and some heavily crosslinked X-MP4-T045 samples, namely X-MP4-T045-23/88 and X-MP4-T045-32/82, the SAXS feature of the tubular structure is still clearly present in the failed crushed samples. In other samples, most notable in X-MP4-T045 (11/94 and 12/88), X-MP4-T065 and X-MP4-T090 (with 11/94 crosslinking formulation), the signature of the tubular nanostructures inside the fundamental nanoworms has been completely lost, in agreement with the results of TEM. Therefore, in those samples, the nanoworms have been crushed, and the fact that the skeletal density is the same throughout compression suggests that indeed all worms were dense objects, filled completely with polymer with no voids or otherwise empty space. Furthermore, we note that as the strain increased, the nanotubular structure expanded:  $d$ -spacing and consequently  $\alpha_0$  values increased. As we have discussed before [10], because of H-bonding among –OH groups inside the tubes, the tubular structure of the native aerogel contracts relative to the structure of the corresponding wet gel ( $d$ -spacing decreases from 126 to 90 Å—see Table 3 and Table 6). That contraction at the nanolevel is higher than that observed at the micro-level. Crosslinking polymer fills the tubes and partially halts that contraction at the nano-level but not completely (the  $d$ -spacing in the X-MP4-T045 sample is 115 Å). Ball-milling the X-MP4-T045 samples destroyed the micro-structure, relieving stresses and tubes expand to  $d$ -spacing of 130 Å. It is suggested that in some cases that expansion leads to the expansion that destroys the tubular structure (e.g., X-MP4-T045-11/94 samples).

By the same token, with heavier crosslinking (i.e., adding more polymer—cases of X-MP4-T045-23/88 and X-MP4-T045-32/82 samples), the  $d$ -spacing remains the same as in the X-MP4-T045-11/95 samples (about 115 Å). It means that the tubes have been completely filled; therefore, the additional polymer spills out of the tubes and coats the nanoworms that define the honeycomb-like macropores. Ultimately, with the nanoworms conformally coated with polymer, they do not burst when the material fails. Thus, we observe an expansion way beyond the spacing even in the original native wet gels (163 vs. 126 Å, respectively), but the tubular nanostructure persists.

### 3.3.9 Surface deformation measurements using DIC

During quasi-static compression tests, a high-speed camera was used to acquire images as the samples were being compressed to help track the deformation process. The

acquired images were then used for digital image correlation measurements (DIC), a non-contact method that implement second-order shape functions as described by Lu and Cary [21] to determine the surface strain distribution. Figure 11a shows the reference undeformed image used to compare with those of the deformed images in Figs. 11b–f. A rectangular segment of the images with a size of 240 × 48 pixels was selected for DIC analysis on each image, with a resolution of 81.50 μm/pixel. It was assumed that for a thin strip of the image that was about 3.9 mm wide, the effects of cylindrical curvature on the deformation measurement were negligible [21, 28]. Figure 13a–e shows the contours of the axial compression strain as determined from the DIC code on the five images shown in Figs. 11b–f. The axial strain started at both the top and bottom ends of the samples and spread toward the middle as strain increased. The transverse compressive strain was also measured by DIC and strain fields are shown in Figs. 13f–j. Along the y-axis, there was higher strain in the middle of the sample that continued to build up as the sample deformed.

The axial strains determined from quasi-static compression data and from DIC (marked by “DIC”) were synchronized with the stress–strain data and are plotted in

Fig. 12. Both the axial and transverse strains have the same slope as the slope of the stress–strain curve at the elastic range up to about 5 % strain. The axial strain data from DIC tracked closely the stress–strain curve up to about 40 %, while the transverse strain started to diverge after the yield point. At about 60 % compressive strains, as shown in Fig. 11g, black speckle dots were compacted too close together to be distinguished so that the grayscale pattern changed significantly and DIC could not be used from that point on. Consequently, after 75 % strain (Fig. 11g), deformations could no longer be calculated from DIC analysis. Figure 12 shows that the data points obtained from DIC analysis agree well with data obtained from the Instron machine, providing further assurance on the validity of the compression data obtained at low strain rates. The Poisson’s ratio was determined as  $0.308 \pm 0.003$  in the linear regime by computing the negative ratio of transverse strain to axial strain, all within the linear regime.

### 3.4 DMA results

The complex modulus data of the X-MP4-T045 in a three-point bending configuration were determined as previously described for a temperature sweep between −121 °C and

**Table 7** Physical properties of crosslinked surfactant-templated silica aerogels with varying concentrations of the swelling agent (TMB) after quasi-static compression at the ultimate strains for each sample (strain rate ~ 0.45 s<sup>-1</sup>)

Sample	% Strain	Bulk density, $\rho_b$ (g/cm <sup>3</sup> )	Skeletal density, $\rho_s$ (g/cm <sup>3</sup> )	Porosity, $\Pi$ (% v/v) <sup>a</sup>
X-MP4-T010	59.0	0.81	1.306	38
X-MP4-T030	8.6	0.67	1.307	49
X-MP4-T045	85.0	0.90	1.267	29
X-MP4-T065	78.5	0.91	1.277	29
X-MP4-T090	83.3	0.96	1.252	23
X-MP4-T125	75.0	0.96	1.238	22
X-MP4-T200	63.0	0.90	1.279	30

All samples were of the −11/94 formulation, namely samples were crosslinked with 11 g of Desmodur N3200 dissolved in 94 mL of dry acetone. All samples were dried from pentane

<sup>a</sup> Porosity  $\Pi = 100 \times (\rho_s - \rho_b) / \rho_s$

**Table 8** Evolution of the physical properties of the X-MP4-T045 samples compressed quasi-statically (strain rate ~0.45 s<sup>-1</sup>) at different percent strains

Sample	% Strain	Bulk density, $\rho_b$ (g/cm <sup>3</sup> )	Skeletal density, $\rho_s$ (g/cm <sup>3</sup> )	Porosity, $\Pi$ (% v/v) <sup>a</sup>
Native-MP4-T045	0	0.477	1.965	75.7
X-MP4-T045	0	0.702	1.268	44.6
X-MP4-T045	8.3	0.690	1.294	46.7
X-MP4-T045	23	0.729	1.296	43.7
X-MP4-T045	55	0.851	1.301	34.6
X-MP4-T045	85	0.900	1.267	29.0

All samples were of the −11/94 formulation, namely samples were crosslinked with 11 g of Desmodur N3200 dissolved in 94 mL of dry acetone. All samples were dried from pentane

<sup>a</sup> Porosity  $\Pi = 100 \times (\rho_s - \rho_b) / \rho_s$

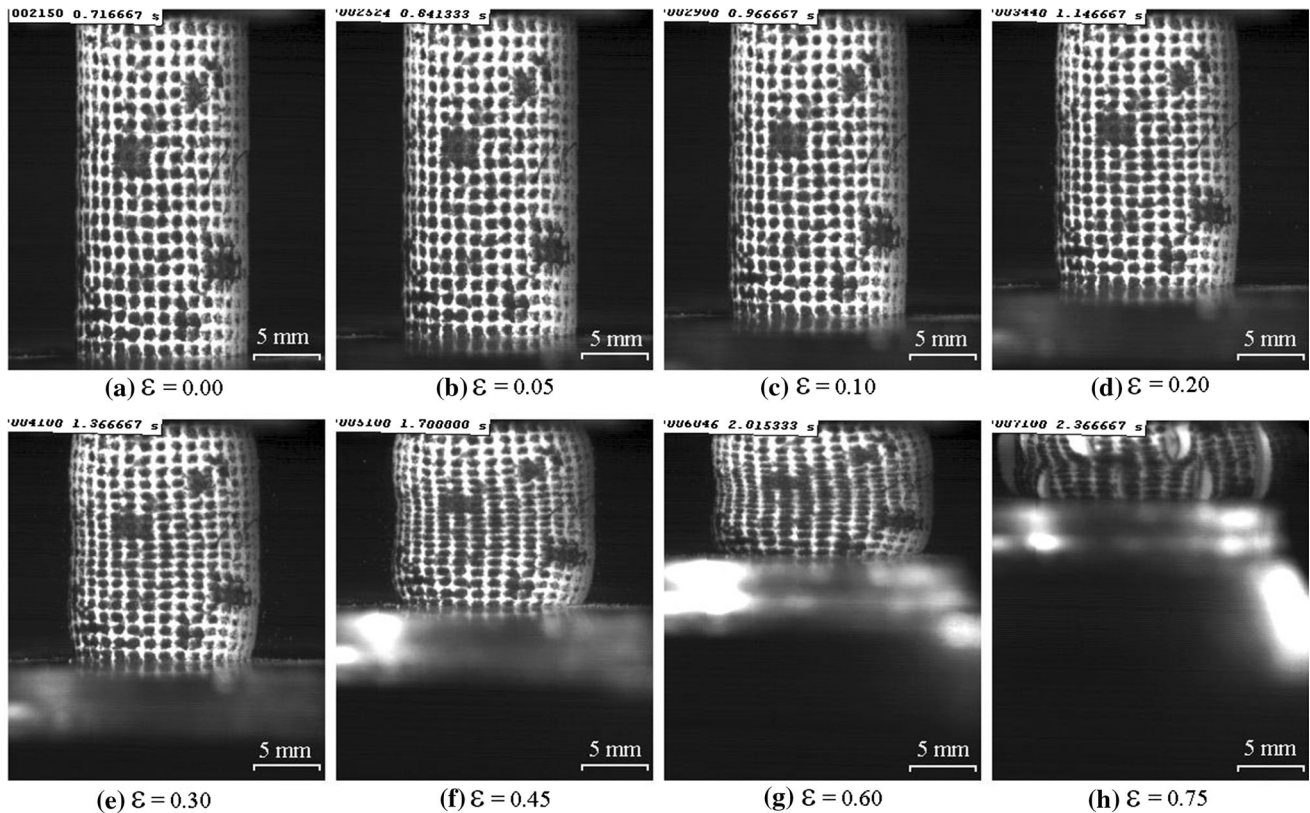


**Fig. 11** High-speed deformation images of X-MP4-T45-11/94 during quasi-static compression. The top platen was fixed and the bottom platen was moved up to compress specimen (units: 81.2  $\mu\text{m}/\text{pixels}$ ).

**a** Initial stage at zero strain, **b** at 5 % strain, **c** at 10 % strain, **d** at 20 % strain, **e** at 30 % strain, **f** at 45 % strain, **g** at 60 % strain and **h** at 75 % strain

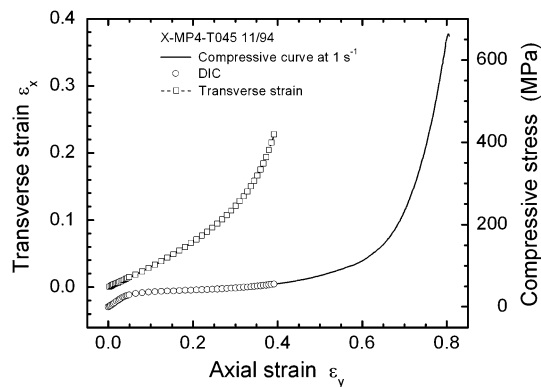


**Fig. 12** Compressive stress–strain curve from quasi-static test data comparing processed machine output from the test with data obtained using DIC images to show how transverse strain and the corresponding axial strain evolve during the test

250 °C at a frequency of 1 Hz with maximum mid-span displacement amplitude of about 0.5 mm. The storage modulus and loss modulus, as well as the loss tangent, are plotted in Fig. 14. The storage modulus decreased as the temperature increased. At  $-121$  °C, the storage modulus was 2.18 GPa, while at room temperature (23 °C), the

storage modulus was 1.11 GPa, decreasing further to 716 MPa at 100 °C. Finally, at 250 °C the storage modulus was 118 MPa. The loss tangent,  $\tan\delta$ , which is the tangent of out-of-phase angle  $\delta$  between stress and strain, was calculated in terms of the ratio of loss modulus to storage modulus. Two peaks marked as “A” and “B” were realized. The primary peak “A” in  $\tan\delta$  occurred about at 150 °C, which is the (primary)  $\alpha$ -glass transition temperature of the X-MP4-T045, while the second peak “B” is at  $-50$  °C, which is  $\beta$ -transition temperature. The  $\alpha$  and  $\beta$  transitions are attributed to the polymer that was used to crosslink the samples. At temperatures above 180 °C, there was a slight shrinkage of about 1 %, but the sample still remained on the knife-edge support, showing that the material had high degree of dimensional stability even at temperature well above 150 °C, which was the estimated glass transition temperature.

### 3.5 Tensile testing

Type II specimens were prepared and tested based on the ASTM D638-10 with the specimen thickness at 3 mm. In tension, the specimens deformed for about 1.2 mm after a

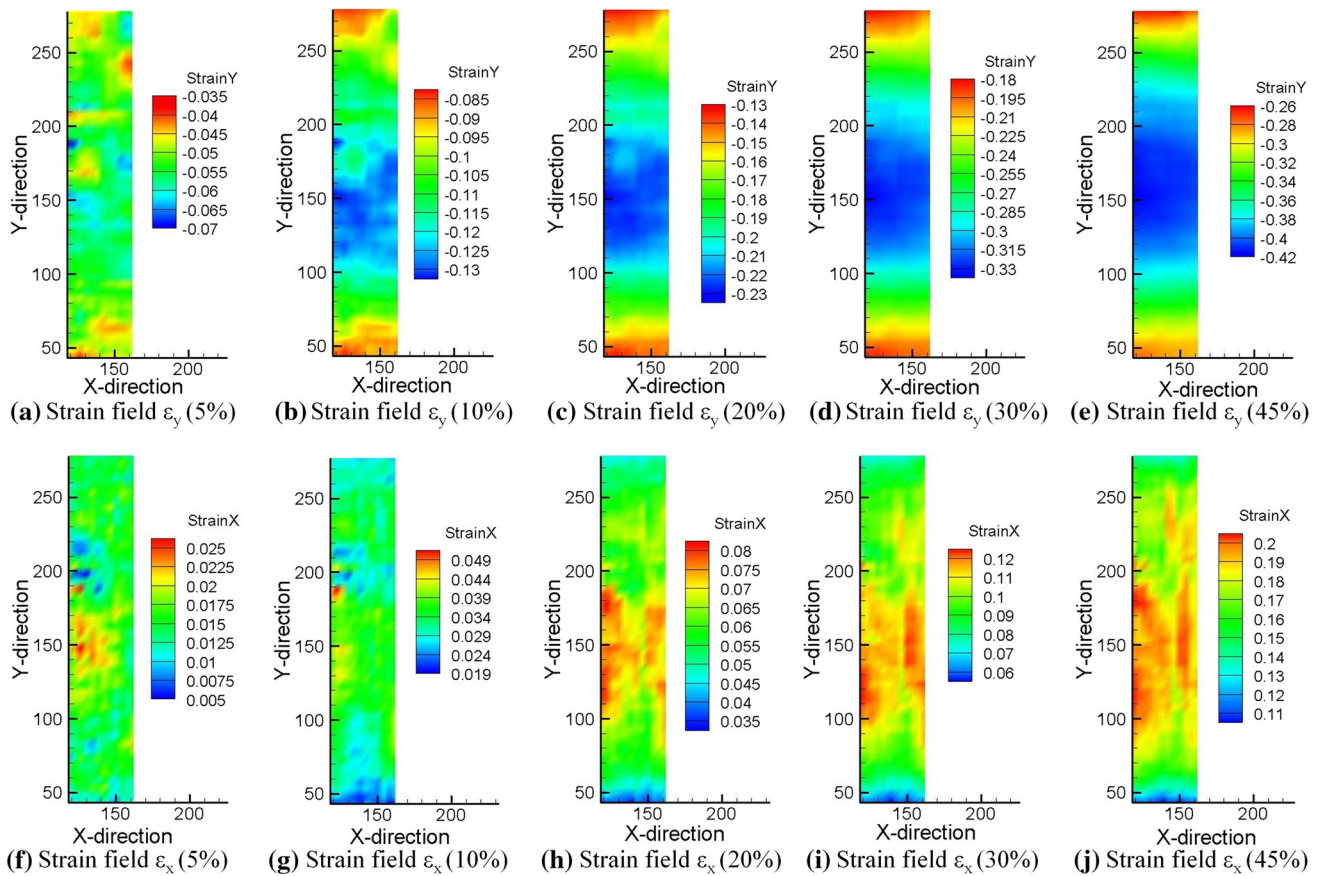


**Fig. 13** Axial and transverse strain field measured using DIC on an area of templated aerogel cylinder of  $3.9 \times 19.5 \text{ mm}^2$  ( $48 \times 240$  pixels; 1 pixel =  $81.15 \mu\text{m}$ ). **a** Axial strain field  $\epsilon_y$  at 5 % global compressive strain. **b** Axial strain field  $\epsilon_y$  at 10 % global compressive strain. **c** Axial strain field  $\epsilon_y$  at 20 % global compressive strain. **d** Axial strain field  $\epsilon_y$  at 30 % global compressive strain. **e** Axial

strain field  $\epsilon_y$  at 45 % global compressive strain. **f** Transverse strain field  $\epsilon_x$  at 5 % global compressive strain. **g** Transverse strain field  $\epsilon_x$  at 10 % compressive strain. **h** Transverse strain field  $\epsilon_x$  at 20 % compressive strain. **i** Transverse strain field  $\epsilon_x$  at 30 % compressive strain. **j** Transverse strain field  $\epsilon_x$  at 45 % compressive strain

load of well over 2.2 kN before a brittle failure occurred as shown in the inset of Fig. 15 with the sample before (left) and after (right) testing. Figure 15 also shows the resulting stress–strain curve with a tensile strength at break of about 19 MPa at 2.3 % strain. These results are unique in that they are rarely reported due to the limitation of the sample size processed for typical aerogels. By using a pentane drying protocol, the size limitation was mitigated to allow for preparation and machining of bigger, slender samples suitable for tensile tests.

### 3.6 High-strain-rate compression testing

Dry and water-soaked CTSA materials were subjected to high-strain-rate impact testing using a SHPB. The strain rate was set in the range of  $210\text{--}3010 \text{ s}^{-1}$ , to study the effect of strain rate during the dynamic test. All samples considered were crosslinked using 11 g of N3200 dissolved

in 94 ml of dry acetone (designated as 11/94). The Young’s modulus, the compressive strength and energy density were found to depend on the amount of swelling agent (TMB) in the sample. Samples that used 0.45 g of the swelling agent (designated as T045) were found to have the most robust mechanical properties as summarized in Table 9 compared with other samples. Figure 16a shows the resulting stress–strain curves. Higher concentrations of TMB (above 0.65 g) resulted in much weaker samples. Considering applications in structural components used within the elastic limit, the stress–strain curves are shifted up, resulting in higher Young’s modulus as well as yield strength (Table 9).

Water-soaked samples were also compressed at similar strain rates and compared to dry samples (Fig. 16b). For the case of X-MP4-T045-11/94, the water in the sample (see Fig. 16b) did not significantly affect the mechanical properties. There was only slight decrease below the curve

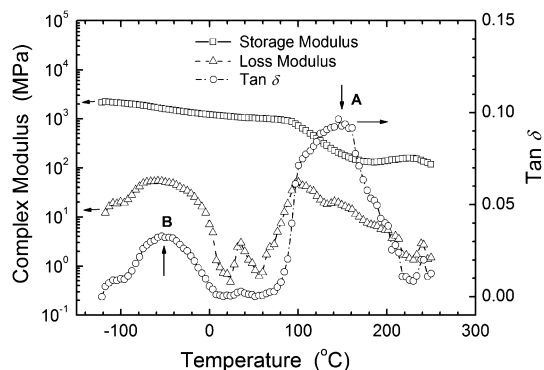


**Fig. 14** DMA test results showing the storage modulus, loss modulus and loss tangent changes as a function of temperature. Loss tangent has two distinct peaks marked as A and B for alpha (primary) glass transition at about 150 °C and beta transition at about -50 °C, respectively

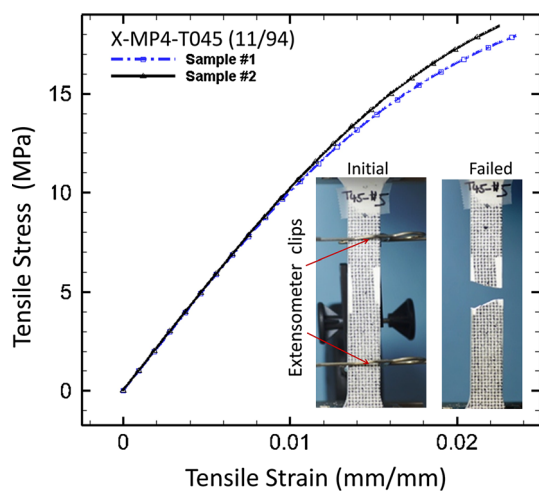


**Fig. 15** Tensile *stress–strain* curve from type II ASTM standard D638-03 tensile specimens for X-MP4-T45 (11/94). *Insert* are Type II ASTM standard D638-03 tensile samples before (*left*) and after (*right*) tensile test. Speckle pattern was applied to the surface to track deformation for digital image correlation analysis

of dry samples, indicating slight decrease in the resulting energy density computed from the area under the stress–strain curve. The behavior within the elastic limit was similar to that of the dry sample. Therefore, it can be concluded that the water content had very little effect on the mechanical strength at high-strain-rate dynamic compression. This is a significant feature since in most cases components and structures are designed to operate within the elastic limit.

The strain rate was varied from 210 to 3010 s<sup>-1</sup>. As the strain rate increased, the stress–strain curve shifted upward (see Fig. 16c), indicating that the material became stronger with the increase of strain rate. This characteristic is a clear indication that the material would be appropriate for energy absorption from high impact projectile such as a bullet.

### 3.7 Shear creep measurement

Figure 17 shows the schematic of the setup used to take the shear creep measurements. Shear creep experiments were performed on two X-MP4-T045 samples (crosslinked with 11/94 formulation), with additional repetition of the shear creep measurement on each. The sample was loaded and tested following the temperature and mechanical loading histories shown in Fig. 18 for the shear creep experiments on aerogel specimens. In summary, the loading and testing cycles included the following: X-MP4-T045 aerogel samples were heated up from room temperature to 110 °C over a period of 3 h, kept at this temperature for 4 h and then gradually cooled to 30 °C over a period of 8 h. Next, testing was continued with loading, unloading and conditioning of the samples at various temperatures. The loading phase lasted 3 h at a constant temperature, then the loading torque was unloaded to zero, and the temperature was increased by 10 °C. The process of heating took approximately 1 h, and then, the specimen was maintained at this new temperature for about 2 h. The specimen was again loaded with torque for 3 h for creep measurements,

**Table 9** Summary of mechanical properties of crosslinked template aerogels under high-strain-rate dynamic tests using modified split Hopkinson pressure bar (SHPB)

Sample	Bulk density (g/cm <sup>3</sup> )	Young's modulus (MPa)	Compressive strength (MPa) <sup>a</sup>	Specific energy density (J/g) <sup>b</sup>
X-MP4-T045	0.69 ± 0.01	768 ± 00	25.0 ± 0.0	84.0 ± 0.0
X-MP4-T065	0.66 ± 0.01	700 ± 52	22.0 ± 0.0	76.5 ± 2.5
X-MP4-T085	0.64 ± 0.01	418 ± 55	12.5 ± 0.5	70.5 ± 3.5
X-MP4-T090	0.73 ± 0.01	525 ± 16	16.0 ± 1.0	84.0 ± 1.0
X-MP4-T125	0.81 ± 0.02	492 ± 57	18.5 ± 0.5	100.0 ± 1.0
X-MP4-T200	0.67 ± 0.01	246 ± 32	8.5 ± 0.5	49.0 ± 1.0

All samples were crosslinked using 11 g of N3200 dissolved in 94 ml of dry acetone

<sup>a</sup> at 5 % strain; <sup>b</sup> computed at 75 % strain

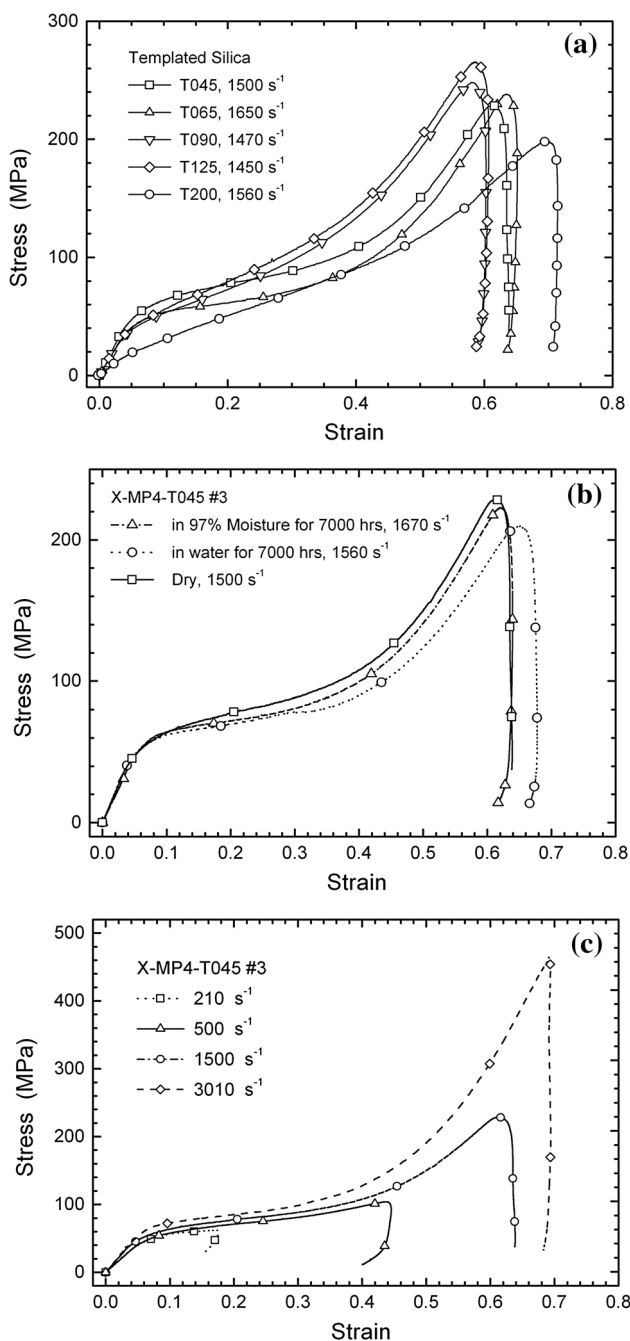


**Fig. 16** High-strain-rate compressive *stress–strain* curves of cross-linked templated silica aerogels. All samples were crosslinked using a solution made of 11 g of N3200 dissolved in 94 ml of acetone. **a** Effect of concentrations of the swelling agent (TMB). **b** Effect of the moisture content. **c** Effect of changing strain rate

and the procedure was repeated over the entire temperature range from 29 to 96 °C in intervals close to 10 °C.

The measured twist angle as a function of time was converted to shear strain in order to calculate the shear creep compliance. The creep behavior was characterized at eight temperatures, and the actual temperature on the

specimen surface was measured. The corresponding shear creep compliance functions at the eight temperatures are shown in Fig. 19a. For a linear viscoelastic material, a master curve can be constructed by shifting curves obtained at different temperatures along the log-time axis with respect to the curve at the reference temperature, to extend the time range at the reference temperature. The temperature at 76 °C was chosen as the reference temperature. The creep compliance master curve (Fig. 19b) was obtained based on time–temperature superposition principle. The inset in Fig. 19b shows the amount of shifting along the log-time axis recorded as a function of the temperature, namely the logarithmic shift factor,  $\log_{10}(a_T)$ . Figure 19c shows shear creep compliance as function of temperature at the selected reference time of  $t_{ref} = 10,000$  s (about 3 h). For the temperature range from 29 to 60 °C, the difference in creep compliance after 3 h is not significant (within 5 %), while in the temperature range from 60 to 100 °C the isochronal shear creep compliance becomes much more temperature sensitive. The isochronal shear creep compliance at 100 °C can be up to 170 % larger than that of 30 °C. In future work, the shear creep master curve can be correlated with the complex modulus measured by DMA through the interconversion of linear viscoelastic properties. The viscoelastic functions will also be used to explain the viscoelastic behavior of the negative stiffness in the loading–unloading compression and further to simulate the microstructure–mechanical properties relationship using numerical methods such as the material point method under complex loading conditions using the viscoelastic constitutive law [28, 29]. Thus, time-dependent nature of aerogels requires further investigations.

### 4 Conclusion

Strong and stiff nano/microporous crosslinked templated silica aerogels were synthesized using a sol–gel process with triblock copolymer Pluronic P123 as a structure-directing agent and TMB as a micelle-swelling reagent. Pluronic P123 was used to regulate the size and shape of the pores, while the concentration of TMB was varied to produce different meso/nanoporous structures, by varying the size, shape and distribution of micelles in the sol. Consequently, the changes in morphology resulted in aerogels that had differing mechanical and physical characteristics. A pentane drying protocol under ambient pressure replaced the traditional supercritical drying, thus eliminating the need for a high pressure autoclave, and therefore, large pieces of aerogels were fabricated and tested. The effect of varying the TMB concentration as well as the crosslinking agent concentration (Desmodur N3200) on the mechanical behavior was investigated and



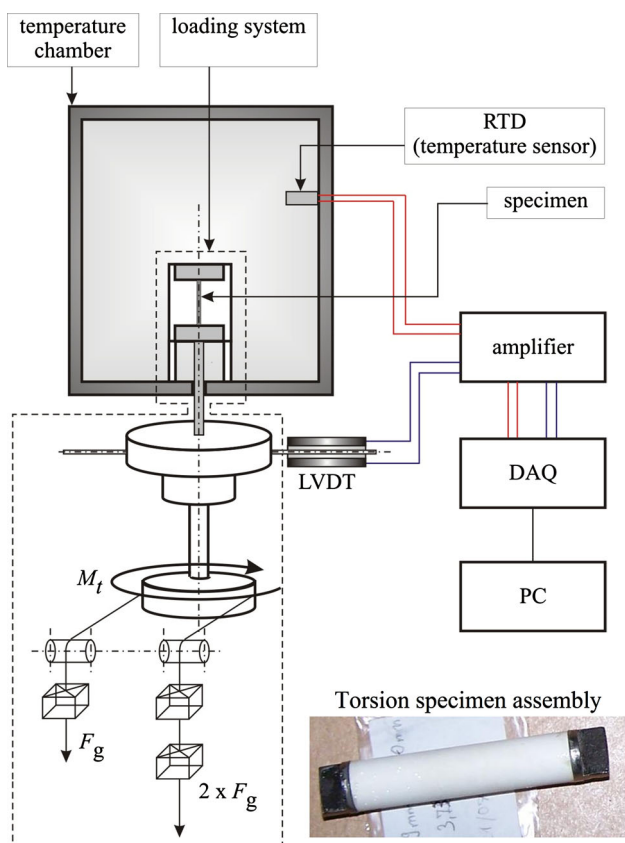


**Fig. 17** Scheme of shear creep torsionmeter. *Inset* (at the bottom right) is the torsion specimen assembly of crosslinked templated silica aerogel specimen, glued to metal holders in preparation for shear creep measurement

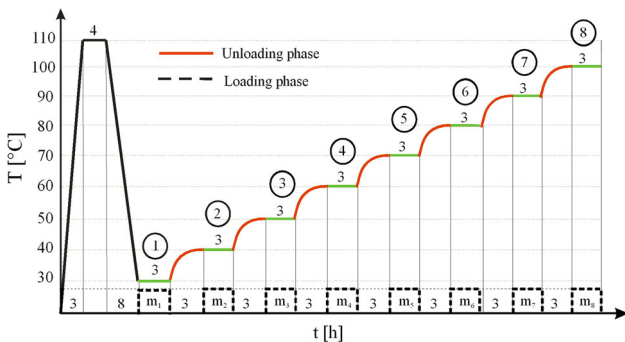


**Fig. 18** Schematic presentation of the temperature and mechanical loading profile during the shear creep measurement of the CTSA specimens

revealed how the morphological changes affected the mechanical as well as the physical properties of these aerogels. In addition, by using an ambient pressure drying protocol by solvent exchange with pentane rather than expensive and size limiting supercritical drying, robust monoliths were synthesized, similar to the ones dried via a

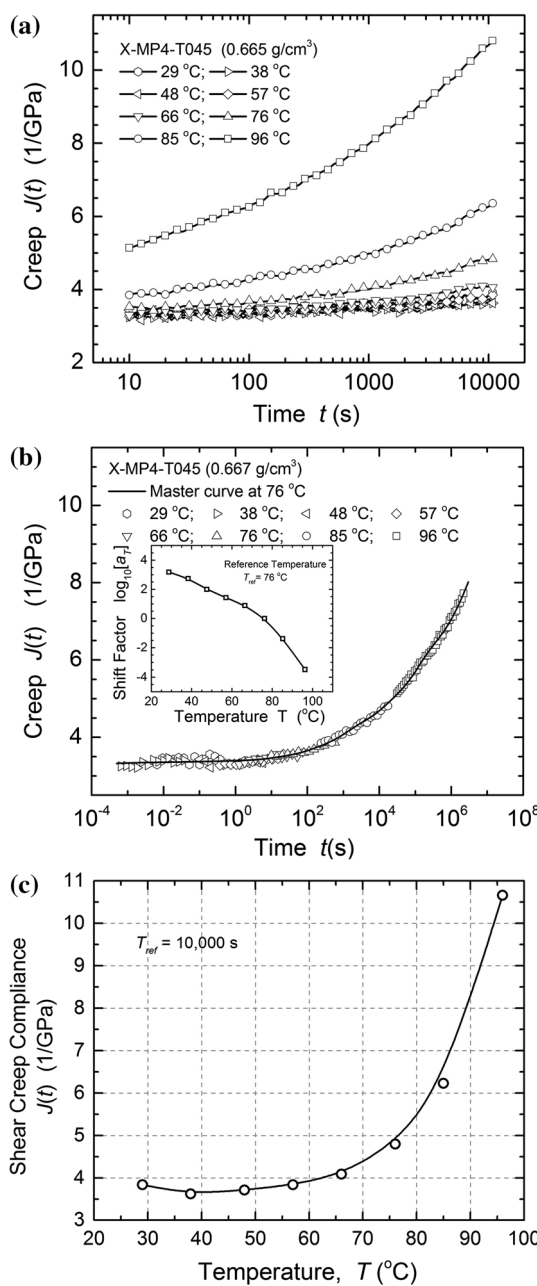


**Fig. 19** Shear viscoelastic behavior of X-MP4-T045. **a** Shear creep compliance at different temperatures. **b** *Shear creep master curve* with *inset* showing the shift factor curve. **c** Shear creep compliance as a function of temperature at the reference time  $t_{ref} = 10,000$  s

supercritical CO<sub>2</sub> drying protocol. Pentane-dried samples had the same microstructure as revealed in SEM images as well as similar mechanical and physical properties. A structurally optimized honeycomb-like structure was obtained with the formulation designated as X-MP4-T045. That material had very a high energy absorption capability, with specific energy absorption reaching 123 J/g, which is much higher value than most man-made materials. DMA indicated that the material had good viscoelastic properties,

with a primary glass transition temperature of about 150 °C. At all strain rates, the effect of moisture absorption on mechanical properties was negligible while low temperature tests showed that even at cryogenic temperatures, the material was still capable of absorbing significant amount of energy under compressive loading. A similar trend was observed when the material was subjected to high-strain-rate compression using a SHPB, indicating potential applications in ballistic protection such as helmets, body and vehicle armor, as well as personnel protective equipment. Overall, a clear correlation between the nano/mesostructure and the mechanical properties has been established, and they can both be tailored by the underlying synthetic conditions.

**Acknowledgments** This project was supported by the Army Research Office under Award No. W911NF-14-1-0369; NSF grants CHE-0809562, CMMI-0653919, CMMI-0653970, DMR-0907291, CMMI-1031829, CMMI-1132174 and ECCS-1307997; and DOE NEUP 09-818. We thank Bayer Corporation USA for the generous supply of Desmodur N3200 and the Materials Research Center of MS&T for support with material characterization.

## References

- Fricke J, Emmerling A (1992) Aerogels-preparation, properties, application, structure and bonding 77. Springer, Berlin, pp 37–87
- Norris PM, Shrinivasan S (2005) *Ann Rev Heat Transf* 14:385–408
- Geis S, Fricke J, Löbmann P (2002) *J Eur Ceram Soc* 22:1155–1161
- Tanaka N, Kobayashi H, Ishizuka N, Minakuchi H, Nakanishi K, Hosoya K, Ikegami T (2002) *J Chromatogr A* 965:35–49
- Rubenstein DA, Lu H, Mahadik SS, Leventis N, Yin W (2012) *J Biomater Sci-Polym* 23:1171–1184
- Yin W, Rubenstein DA (2011) Biomedical applications of aerogels. In: Aegerter M, Leventis N, Koebel M (eds) *Aerogels handbook*. Springer, New York, pp 683–694
- Leventis N, Sotiriou-Leventis C, Zhang G, Rawashdeh AM (2002) *Nano Lett* 2:957–960
- Leventis N, Vassilaras P, Fabrizio E, Dass A (2007) *J Mater Chem* 17:1502–1508
- Leventis N, Palczer A, McCorkle L, Zhang G, Sotiriou-Leventis C (2005) *J Sol-Gel Sci Technol* 35:99–105
- Katti A, Shimpi N, Roy S, Lu H, Fabrizio EF, Dass A, Capaduna LA, Leventis N (2006) *Chem Mater* 18:285–296
- Vartuli JC, Schmitt KD, Kresge CT, Roth WJ, Leonowicz ME, McCullen SB, Hellring SD, Beck JS, Schlenker JL, Olson DH, Sheppard EW (1994) *Surf Sci Catal* 84:53–60
- Vartuli JC, Roth WJ, Beck JS, McCullen SB, Kresge CT (1998) *Mol Siev* 1:97–119
- Scott BJ, Wirmsberger G, Stucky G (2001) *Chem Mater* 13:3140–3150
- Amatani T, Nakanishi K, Hirao K, Kodaira T (2005) *Chem Mater* 17:2114–2119
- Nakanishi K, Takana N (2007) *Acc Chem Res* 40:863–873
- Nakanishi K, Amatani T, Yano S, Kodaira T (2008) *Chem Mater* 20:1108–1115
- Leventis N, Mulik S, Wang X, Dass A, Patil VU, Sotiriou-Leventis C, Lu H, Churu G, Capececiatro A (2008) *J Non-Cryst Solids* 354:632–644
- Leventis N, Mulik S, Wang X, Dass A, Sotiriou-Leventis C, Lu H (2007) *J Am Chem Soc* 129:10660–10666
- Luo H, Lu H, Leventis N (2006) *Mech Time-Depend Mater* 10:83–111
- Luo H, Churu G, Fabrizio EF, Schnobrich J, Hobbs A, Dass A, Mulik S, Zhang Y, Grady BP, Capececiatro A, Sotiriou-Leventis C, Lu H, Leventis N (2008) *J Sol-Gel Sci Technol* 48:113–134
- Lu H, Cary PD (2000) *Exp Mech* 40:393–400
- Metlikovič P, Emri I (1994) *Kovine Zlitine Tehnologije* 28:407–409
- Metlikovič P (1989) Analiza procesa lezenja viskoelastičnih materialov pod vplivom strižne obremenitve, magistrska naloga. Fakulteta za strojništvo, Ljubljana
- Metlikovič P, Emri I (1989) *Stroj Vestn* 35:56–58
- Metlikovič P, Emri I (1990) *Stroj Vestn* 36:101–104
- Cvelbar R, Emri I (1994) *Kovine Zlitine Tehnologije* 28:359–362
- Stringari GB, Zupančič B, Kubyskhina B, von Bernstorff B, Emri I (2011) *Powder Technol* 208:590–595
- Daphalapurkar NP, Hanan JC, Phelps NB, Bale H, Lu H (2008) *Mech Adv Mater Struct* 15:594–611
- Fu B, Luo H, Wang F, Churu G, Chu KT, Hanan JC, Sotiriou-Leventis C, Leventis N, Lu H (2011) *J Non-Cryst Solids* 357:2063–2074